# A Stretched Grid Finite Difference Time-Domain Scheme Implemented With Anisotropic Perfectly Matched Layer

Xiaojun Huang, Yibing Zheng, Daniel R. Burns, and M. Nafi Toksöz,
Earth Resources Laboratory
Dept. of Earth, Atmospheric, and Planetary Sciences
Massachusetts Institute of Technology
Cambridge, MA 02139

**Abstract**

A stable 2.5D finite difference time-domain (FDTD) scheme is developed to study wave propagation in heterogeneous media. One example is the logging while drilling configuration where small features such as the annulus between the drill pipe and the formation, only about 1/10 or even smaller than the wavelength in the steel pipe, affect the wave field significantly. The FDTD scheme proposed in this paper improves computational efficiency and accuracy from three aspects: griding, differencing, and numerical truncation. Coordinate stretching, proving to be more accurate, stable, and easy to implement, is employed to achieve variable griding. A wavelet-based differencing scheme is derived and compared with conventional FDTD schemes with spatial truncation accuracy being 2nd, 4th, 6th and 8th order. Because the wavelet-based and higher order FDTD scheme exhibits highly linear dispersion properties, it allows coarser griding and is therefore more efficient. Reflections and transmission coefficients estimated from all FDTD schemes at a sharp boundary show that the wavelet-based FDTD solution outperforms the others. Efficient numerical truncation is realized by an anisotropic perfectly matched layer.

## 1 Introduction

In order to extract information about the earth from acoustic logging observations, it is necessary to predict how wave-fields are affected by complex borehole-tool structures. Since exact solutions to the wave equations do not exist for most logging configurations, numerical simulation becomes the only viable approach to estimate such solutions.

Synthetic seismograms obtained from numerical simulation help us to predict and understand the kinematic and dynamic properties of seismic/acoustic waves propagating in the earth. They also help to determine optimal recording parameters in data acquisition and evaluate processing schemes in data processing.

Various techniques for wave modeling in complex media have been developed. Such methods include wavenumber integration, e.g. the reflectivity method (Muller, 1985), ray-tracing (Cerveny, 2001), finite elements (Chen, 1984), Fourier or pseudo-spectral methods (Kosloff and Baysal, 1982), hybrid methods (Emmerich, 1992), and finite differences (FD) (Alterman and Karal, 1968).

The FDTD method has been one of the most powerful tools to simulate wave propagation in 2-D or 3-D elastic media because it can model wave propagation accurately in arbitrarily heterogeneous media. Kelly et al. (1976) used a displacement formulation developed from the second-order elastic equations. Levander (1988) formulated a staggered-grid, finite difference scheme based on a system of first-order coupled elastic equations where the variables are stresses and velocities, rather than displacements.

Over the past 20 years, as computer capacity increased exponentially, numerical simulation using finite difference can handle more sophisticated models, from seismic wave propagation in a basin with a realistic structure, to electromagnetic wave propagating in optical fibers with fine details. However, a stable and accurate FDTD scheme with a realistic bandwidth requires a certain number of grid points per wavelength. Therefore, even with the most updated computational facilities that have dozens of central processing

units(CPU) and gigabytes of memory, we are still unable to simulate efficiently most models to a satisfactory level, such as wave propagation in the logging while drilling (LWD) configuration.

The FDTD scheme developed in this paper will be used primarily to investigate wave propagations in the LWD situation. A major difficulty of using the FDTD method to simulate wave propagation in the LWD situation is that small features, like the annulus between the drill pipe and the formation, affect wavefield significantly but are only about 1/10 of the wavelength in the steel pipe. At least three points are required to show the effect of the annulus, and that results in a redundent griding for the rest of the model if using uniform grids. The purpose of our research, therefore, is to improve the efficiency of FDTD schemes without losing if not improving the accuracy. We examine this from three perspectives: the griding scheme, the FD operator and the numerical absorbing boundary.

## 2 Non-Uniform Grid via Coordinate Stretching

While the FDTD method developed on a uniform grid may be the simplest and most accurate scheme (Cjemg, 1994; Randall, 1991), it can be highly deficient in some respects. When modeling wave propagation along a fluid-filled borehole with a drilling pipe inside, if the grid size is not small enough to capture the thin annulus between the tool and the formation, the FDTD solution can poorly reflect the characteristics of guided modes and the coupling between them. However if the grid size is small enough to simulate the annulus, the number of grids for the whole model is far more than necessary, thus making the FDTD algorithm unnecessarily expensive to compute, including memory requirements and running time.

To avoid excessive numbers of calculations, while still obtaining a high degree of resolution in some particular regions, a non-uniform grid system may be used with a fine grid in the borehole area with small features or large changes and coarse grid over the rest of the areas that are smooth. There have been several different types of non-uniform grids applied to solve partial differential equations (PDEs). For example, it is possible to have a coarse grid that changes abruptly to a fine grid (Hayashi, 1999; Lilla, 1997), or it is possible to have a grid that changes gradually to a smaller size grid in the region of interest Anthes, 1970; Harrison, 1973).

While there are considerable benefits to be gained by having a non-uniform grid, these may be offset by other problems introduced by the change in grid size. There may be wave distortion due to a phase change at the interface of two grids or numerical reflections off the interface (Browning et al., 1973). While numerical reflection can be eliminated by taking extra averages of solutions at the grid interface, wave distortion is hard to avoid. It may also be difficult to match and implement the finite difference approximations at the interface of different grids (Hayashi, 1999; Lilla, 1997). The introduction of a change in grid spacing may also adversely affect the formal truncation error and the stability of the system (Crowder and Dalton, 1971).

Because of these difficulties, a coordinate transformation, or stretching, may be preferred to achieve an effective change in grid size. By transforming independent coordinate variables into another domain, non-uniform grid spacing is obtained in the physical domain, while uniform grid spacing is obtained in the transformed domain. Since finite difference approximation is conducted in the transformed domain where grid spacing is uniform, problems associated with non-uniform grid are eliminated naturally. Meanwhile, as grid spacing in the physical domain is non-uniform, the advantage of using non-uniform grid (saving memory and running time) is maintained. There have been several successful applications of finite difference approximation using coordinate transformation. For example, Kalnay de Rivas achieved a large improvement in accuracy when simulating the circulation of the atmosphere on Venus (Kalnay de Rivas, 1972). However, little effort has been put into solving elastic wave equations with finite difference approximation using coordinate transformation.

In this section, we will construct a stretching grid finite difference approximation for the elastic wave equations.

Coordinate stretching is a coordinate transformation that maps the physical domain, $\vec{x} = [x_1, x_2, x_3]^T$, to the transformed or stretched domain, $\tilde{\vec{x}} = [\tilde{x}_1, \tilde{x}_2, \tilde{x}_3]^T$, by a grid mapping function $\epsilon^i(\tilde{x}_i)$, where $i = 1, 2, 3$, representing three orthogonal coordinate directions. $\epsilon^i(\tilde{x}_i)$ should be differentiable with respect to $\tilde{x}_i$, at least to the order of the PDE that is to be solved. $\epsilon^i(\tilde{x}_i)$ is constructed in the manner that the grid spacing in the stretched coordinate, $d\tilde{x}_i$, is uniform whereas grid spacing in the physical coordinate, $dx_i$ is non-uniform.

$$dx_i = \epsilon^i(\tilde{x}_i)d\tilde{x}_i \tag{1}$$

In this paper, $\epsilon^i(\tilde{x}_i)$ is built as follows:

$$\epsilon^i(\tilde{x}_i) = \begin{cases} 1 & \tilde{x}_i \leqslant \tilde{x}_i^0 \\ 1 + (\alpha - 1)\sin\frac{\pi}{2L}(\tilde{x}_i - \tilde{x}_i^0) & \tilde{x}_i^0 \leqslant \tilde{x}_i \leqslant \tilde{x}_i^0 + L \\ \alpha & \tilde{x}_i \geqslant \tilde{x}_i^0 + L \end{cases} \tag{2}$$

where $\alpha$ is the stretching parameter that controls the effective velocity in the transformed domain. It is also the ratio between the coarse and the fine grid in the physical domain. Note that unlike the abrupt grid changing scheme Hayashi, 1999; Lillas, 1997), $\alpha$ does not have to be an integer. $L$ is the transition length. Figure 1 shows the shape of the stretching function, $\epsilon(\tilde{x})$. When $\epsilon$ is 1, $dx = d\tilde{x}$, the grid spacing

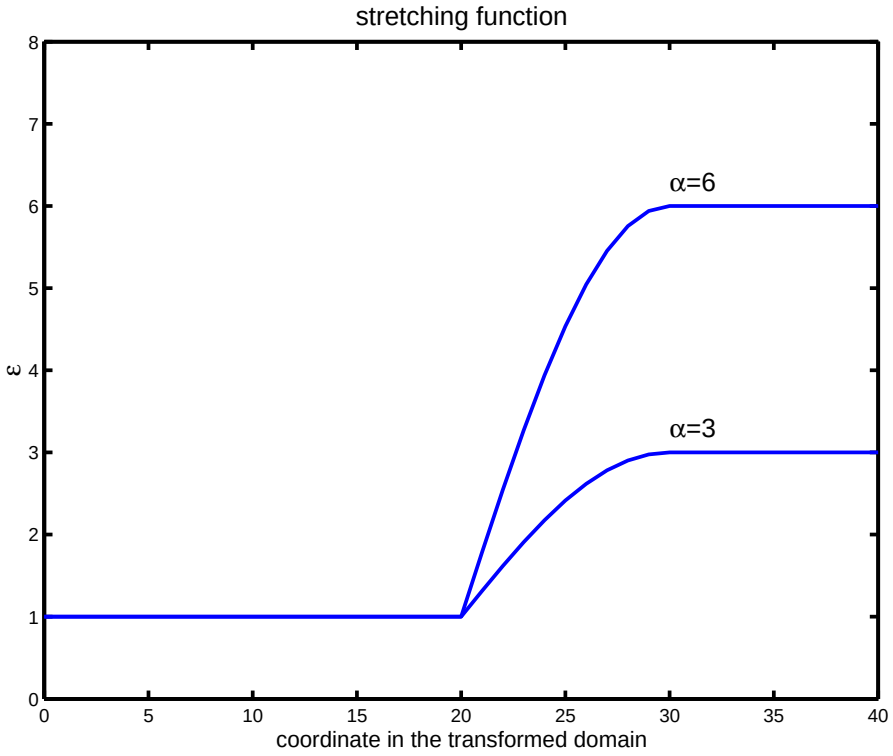


Figure 1: The stretching function $\epsilon(\tilde{x})$ for different stretching parameters.

in the physical domain is the same as in the transformed domain. When $\epsilon$ takes some other value, the grid spacing in the physical domain is $\epsilon$ times larger than it in the transformed domain; therefore, grid spacing in the physical domain is non-uniform, whereas it is uniform in the transformed domain. The wave equations are then solved in the transformed domain using finite difference approximation with uniform griding, thus avoiding the problems that occur with non-uniform grids.

Integrate equation 1, the explicit mapping relation between the physical domain $\vec{x} = [x_1, x_2, x_3]^T$ and the stretching domain $\vec{\tilde{x}} = [\tilde{x}_1, \tilde{x}_2, \tilde{x}_3]^T$ is established as

$$x_i = \begin{cases} \tilde{x}_i & \tilde{x}_i \leqslant \tilde{x}_i^0 \\ \tilde{x}_i + (\alpha - 1)\frac{2L}{\pi}\{1 - \cos\frac{\pi}{2L}(\tilde{x}_i - \tilde{x}_i^0) & \tilde{x}_i^0 \leqslant \tilde{x}_i \leqslant \tilde{x}_i^0 + L\} \\ (1 - \alpha)(\tilde{x}_i^0 + L - \frac{2L}{\pi}) + \alpha\tilde{x}_i & \tilde{x}_i \geqslant \tilde{x}_i^0 + L \end{cases} \tag{3}$$

Figures 2 and 3 illustrate grid spacing in both domains. The figures show that the model space becomes smaller after coordinate transformation, requiring less memory and running time. Applying the chain rule,

the elastic wave equations after the coordinate transformation can be written as,

$$\rho v_{j,t} = \frac{1}{\epsilon^{\alpha}(\tilde{x}_{\alpha})} \tau_{\alpha j,\alpha} \tag{4}$$

$$\tau_{\alpha j,t} = c_{\alpha j \gamma \beta} \frac{1}{\epsilon^{\beta}(\tilde{x}_{\beta})} v_{\gamma,\beta} \tag{5}$$

where $\alpha$, $j$, $\gamma$ and $\beta$ take the values of 1, 2 and 3. Equations 4 and 5 show that the effective wave velocity is slower in the transformed domain, which is compensated by a smaller model size; hence the total travel time is the same as in the physical domain.

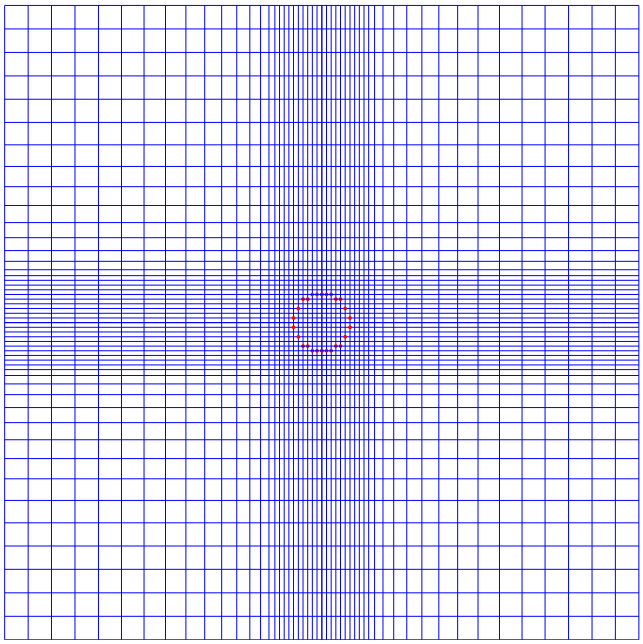

Figure 2: Non-uniform grid spacing in the physical domain. The stretching ratio is 5.

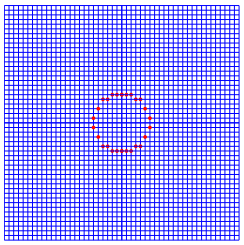

Figure 3: Uniform grid spacing in the transformed domain. Comparing to Figure 2, the model space becomes much smaller thus saving memory and running time.

## 3 Anisotropic Perfectly Matched Layer

In most cases, we need to simulate wave propagations in a boundless medium, hence the medium is truncated into a finite size. This requires numerically implementing an absorbing boundary layer surrounding the

computational domain to reduce reflections off the numerical boundary. An inefficient absorbing boundary layer results in a less accurate and less efficient algorithm.

Berenger (1994) first proposed the perfectly matched layer (PML) concept for electrodynamics using the FDTD method. Different from most traditional or differential equation-based absorbing boundaries, the PML satisfies all continuity conditions at the interface between the computational domain and the PML. Therefore, it has proven to be the most efficient mechanism to absorb wave energies outside the computational domain (Taflove, 1998). Liu formulated the PML for elastic waves using the field-splitting method which requires 27 independent unknowns for a general 3-D problem (9 velocity components and 18 stress components), three times the original 9 variables in ordinary elastic wave equations (Liu, 1999). Zheng and Huang formulated an anisotropic PML without using field splitting that only requires 12 independent unknowns for a general 3-D problem, and showed superior results using the finite element method (Zheng and Huang, 2001). In this paper, further study shows that 21 independent unknowns are required for a stable FDTD PML.

Suppose that any real medium where a plane wave is traveling with a wavenumber $\vec{k}$, its perfectly matched layer is an artificial medium where the same plane wave travels with a complex wavenumber $\vec{k^p}$, the real part of that wavenumber $\mathrm{Re}(\vec{k^p})$ equals to $\vec{k}$. If the medium and its perfectly matched layer are placed next to each other, there will be no reflections or other transmissions generated (Taflove, 1998). Since the wavenumber is complex, the plane wave is attenuated inside the PML. Because any wave with an arbitrary wavefront can be considered as a linear combination of a set of plane waves traveling in different directions, this wave is also attenuated in the PML and can travel across the real medium and its perfectly matched layer without generating any reflections or other transmissions at the interface. So, if such PMLs can be found for any real media, in numerical computation, we can always put them around the computational domain to simulate wave propagation in a boundless medium.

Zheng and Huang (2001) proved that the PML of any real medium exists and provided a systematic way to find it for general anisotropic media in Cartesian and curvilinear coordinates. It is worth mentioning that PML is usually anisotropic. In this section, PML is derived for a stretched coordinate and applied to the FDTD algorithm.

## 3.1 Formulation

Inside the PML, according to the formulation in Zheng and Huang (2001), equation 4 becomes

$$\rho e_1 e_2 e_3 v_{j,t} = \frac{1}{\epsilon^{\alpha}(\tilde{x}_{\alpha})} \tau^{\mathrm{PML}}_{\alpha j,\alpha} \tag{6}$$

Let tensor $\bar{\bar{\tau}}^{\mathrm{PML}} = \tau^{\mathrm{PML}}_{\alpha j}$, denoting stress components in the PML, it is related to the stress tensor $\bar{\bar{\tau}} = \tau_{\alpha j}$ in the computational domain next to the PML by

$$\bar{\bar{\tau}}^{\mathrm{PML}} = e_1 e_2 e_3 \begin{bmatrix} \frac{1}{e_1} & & \\ & \frac{1}{e_2} & \\ & & \frac{1}{e_3} \end{bmatrix} \bar{\bar{\tau}} \tag{7}$$

Complex numbers $e_1$, $e_2$ and $e_3$ are chosen such that normal and tangential stress components are continuous across the boundary between the computational domain and the PML. Writing every component explicitly in the following, equation 7 shows how stress continuity is achieved.

$$\tau^{\mathrm{PML}}_{xx} = e_2 e_3 \tau_{xx}, \quad \tau^{\mathrm{PML}}_{xy} = e_2 e_3 \tau_{xy}, \quad \tau^{\mathrm{PML}}_{xz} = e_2 e_3 \tau_{xz}, \tag{8}$$

$$\tau^{\mathrm{PML}}_{yx} = e_1 e_3 \tau_{yx}, \quad \tau^{\mathrm{PML}}_{yy} = e_1 e_3 \tau_{yy}, \quad \tau^{\mathrm{PML}}_{yz} = e_1 e_3 \tau_{yz}, \tag{9}$$

$$\tau^{\mathrm{PML}}_{zx} = e_1 e_2 \tau_{zx}, \quad \tau^{\mathrm{PML}}_{zy} = e_1 e_2 \tau_{zy}, \quad \tau^{\mathrm{PML}}_{zz} = e_1 e_2 \tau_{zz}. \tag{10}$$

Let $e_1 = 1 - i\zeta_1$, $e_2 = 1 - i\zeta_2$ and $e_3 = 1 - i\zeta_3$. Suppose elastic waves traveling at all angles hit the numerical boundary with the normal direction coincidence with $x$ coordinate, if $\zeta_2$ and $\zeta_3$ are chosen to be 0 and $\zeta_1$ increases gradually from 0 to some finite number away from the numerical boundary, stress components including normal and tangential components acting on the numerical boundary are continuous across the

boundary, i.e., $\tau_{xx} = \tau_{xx}^{\text{PML}}$, $\tau_{xy} = \tau_{xy}^{\text{PML}}$ and $\tau_{xz} = \tau_{xz}^{\text{PML}}$. Note that the stress tensor in the PML, $\tau_{ij}^{\text{PML}}$ is not symmetric. Details of selecting $e_1$, $e_2$ and $e_3$ will be illustrated in section 5.

In vector and tensor format, equation 5 can be written as two separate equations

$$\begin{bmatrix} \frac{1}{e_2 e_3} & & \\ & \frac{1}{e_1 e_3} & \\ & & \frac{1}{e_1 e_2} \end{bmatrix} \frac{\partial \bar{\bar{\tau}}^{\text{PML}}}{\partial t} = \mathbf{C} : \bar{\bar{E}}^{\text{PML}} \tag{11}$$

$$\begin{bmatrix} e_1 & & \\ & e_2 & \\ & & e_3 \end{bmatrix} \bar{\bar{E}}^{\text{PML}} = \nabla \vec{v} \tag{12}$$

where $\bar{\bar{E}}^{\text{PML}}$ has 9 components, representing the strain rate in the PML. The benefit of dividing equation 5 into equations 11 and 12, and introducing the strain rate, $\bar{\bar{E}}^{\text{PML}}$, is to have a stable and simple FDTD algorithm, far beating the cost of requiring slightly more computation and memory inside PML. Let $e_1 e_2 e_3 = A - iB/\omega$, where $A, B \in \mathbb{R}$, $\omega$ is an arbitrary angular frequency, then Fourier transform equation 6, apply the relationship of $i\omega = 1/\partial t$, and then inverse Fourier transform, in vector form, equation 6 becomes

$$\rho A \partial_t \vec{v} + \rho B \vec{v} = \tilde{\nabla}_v \vec{\tau}^{\text{PML}} \tag{13}$$

where $\vec{v} = [v_x, v_y, v_z]^T$ and $\vec{\tau}^{\text{PML}} = [\tau_{xx}^{\text{PML}}, \tau_{yy}^{\text{PML}}, \tau_{zz}^{\text{PML}}, \tau_{xy}^{\text{PML}}, \tau_{yx}^{\text{PML}}, \tau_{xz}^{\text{PML}}, \tau_{zx}^{\text{PML}}, \tau_{yz}^{\text{PML}}, \tau_{zy}^{\text{PML}}]^T$.

$$\tilde{\nabla}_v = \begin{bmatrix} \frac{1}{\epsilon^1(\tilde{x})}\partial_{\tilde{x}} & 0 & 0 & 0 & \frac{1}{\epsilon^2(\tilde{y})}\partial_{\tilde{y}} & 0 & \frac{1}{\epsilon^3(\tilde{z})}\partial_{\tilde{z}} & 0 & 0 \\ 0 & \frac{1}{\epsilon^2(\tilde{y})}\partial_{\tilde{y}} & 0 & \frac{1}{\epsilon^1(\tilde{x})}\partial_{\tilde{x}} & 0 & 0 & 0 & 0 & \frac{1}{\epsilon^3(\tilde{z})}\partial_{\tilde{z}} \\ 0 & 0 & \frac{1}{\epsilon^3(\tilde{z})}\partial_{\tilde{z}} & 0 & 0 & \frac{1}{\epsilon^1(\tilde{x})}\partial_{\tilde{x}} & 0 & \frac{1}{\epsilon^2(\tilde{y})}\partial_{\tilde{y}} & 0 \end{bmatrix} \tag{14}$$

Following a similar approach, as taken for equation 6, equation 11 becomes

$$\mathbf{\Pi} \vec{\tau}^{\text{PML}} = \mathbf{C} \vec{E}^{\text{PML}} \tag{15}$$

where $\vec{E}^{\text{PML}} = [E_{xx}^{\text{PML}}, E_{yy}^{\text{PML}}, E_{zz}^{\text{PML}}, E_{xy}^{\text{PML}}, E_{yx}^{\text{PML}}, E_{xz}^{\text{PML}}, E_{zx}^{\text{PML}}, E_{yz}^{\text{PML}}, E_{zy}^{\text{PML}}]^T$; Components of matrix $\mathbf{\Pi}$ and $\mathbf{C}$ are listed below.

$$\mathbf{\Pi} = \begin{bmatrix} R\pi^1\partial_t + I\pi^1 & & & & & & & & \\ & R\pi^2\partial_t + I\pi^2 & & & & & & & \\ & & R\pi^3\partial_t + I\pi^3 & & & & & & \\ & & & R\pi^1 + I\pi^1 & & & & & \\ & & & & R\pi^2\partial_t + I\pi^2 & & & & \\ & & & & & R\pi^1\partial_t + I\pi^1 & & & \\ & & & & & & R\pi^3\partial_t + I\pi^3 & & \\ & & & & & & & R\pi^2\partial_t + I\pi^2 & \\ & & & & & & & & R\pi^3\partial_t + I\pi^3 \end{bmatrix} \tag{16}$$

where

$$R\pi^1 = \frac{1 - \zeta_2\zeta_3}{(1 - \zeta_2\zeta_3)^2 + (\zeta_2 + \zeta_3)^2}, \qquad I\pi^1 = -\frac{(\zeta_2 + \zeta_3)\omega}{(1 - \zeta_2\zeta_3)^2 + (\zeta_2 + \zeta_3)^2} \tag{17}$$

$$R\pi^2 = \frac{1 - \zeta_1\zeta_3}{(1 - \zeta_1\zeta_3)^2 + (\zeta_1 + \zeta_3)^2}, \qquad I\pi^2 = -\frac{(\zeta_1 + \zeta_3)\omega}{(1 - \zeta_1\zeta_3)^2 + (\zeta_1 + \zeta_3)^2} \tag{18}$$

$$R\pi^3 = \frac{1 - \zeta_1\zeta_2}{(1 - \zeta_1\zeta_2)^2 + (\zeta_1 + \zeta_2)^2}, \qquad I\pi^3 = -\frac{(\zeta_1 + \zeta_2)\omega}{(1 - \zeta_1\zeta_2)^2 + (\zeta_1 + \zeta_2)^2}. \tag{19}$$

$$\mathbf{C} = \begin{bmatrix} c_{11} & c_{12} & c_{13} & & & & & & & \\ c_{12} & c_{22} & c_{23} & & & & & & & \\ c_{13} & c_{23} & c_{33} & & & & & & & \\ & & & c_{66} & c_{66} & & & & & \\ & & & c_{66} & c_{66} & & & & & \\ & & & & & c_{55} & c_{55} & & & \\ & & & & & c_{55} & c_{55} & & & \\ & & & & & & & c_{44} & c_{44} \\ & & & & & & & c_{44} & c_{44} \end{bmatrix} \tag{20}$$

Similarly, equation 12 becomes

$$\Xi \vec{E}^{\mathrm{PML}} = \tilde{\nabla}_E \vec{v} \tag{21}$$

where

$$\Xi = \begin{bmatrix} -\frac{\zeta_1}{\omega}\partial_t + 1 & & & & & & & & \\ & -\frac{\zeta_2}{\omega}\partial_t + 1 & & & & & & & \\ & & -\frac{\zeta_3}{\omega}\partial_t + 1 & & & & & & \\ & & & -\frac{\zeta_1}{\omega}\partial_t + 1 & & & & & \\ & & & & -\frac{\zeta_2}{\omega}\partial_t + 1 & & & & \\ & & & & & -\frac{\zeta_1}{\omega}\partial_t + 1 & & & \\ & & & & & & -\frac{\zeta_3}{\omega}\partial_t + 1 & & \\ & & & & & & & -\frac{\zeta_2}{\omega}\partial_t + 1 & \\ & & & & & & & & -\frac{\zeta_3}{\omega}\partial_t + 1 \end{bmatrix} \tag{22}$$

and

$$\tilde{\nabla}_E = \begin{bmatrix} \frac{1}{\epsilon^1(\tilde{x})}\partial_{\tilde{x}} & & \\ & \frac{1}{\epsilon^2(\tilde{y})}\partial_{\tilde{y}} & \\ & & \frac{1}{\epsilon^3(\tilde{z})}\partial_{\tilde{z}} \\ & \frac{1}{\epsilon^1(\tilde{x})}\partial_{\tilde{x}} & \\ \frac{1}{\epsilon^2(\tilde{y})}\partial_{\tilde{y}} & & \\ & & \frac{1}{\epsilon^1(\tilde{x})}\partial_{\tilde{x}} \\ \frac{1}{\epsilon^3(\tilde{z})}\partial_{\tilde{z}} & & \\ & & \frac{1}{\epsilon^2(\tilde{y})}\partial_{\tilde{y}} \\ & \frac{1}{\epsilon^3(\tilde{z})}\partial_{\tilde{z}} & \end{bmatrix} \tag{23}$$

Until now, the wave equations in the PML have been derived in the transformed coordinate domain (equations 13, 15 and 21). There are two remarkable properties about those equations. 1) Though orthorhombic anisotropy is assumed throughout the paper, or explicitly specified otherwise, those equations can deal with general anisotropic media, therefore the PML designed using those equations can attenuate numerical energies even when the medium in the computational domain is anisotropic. 2) When the parameters $\zeta_1$, $\zeta_2$ and $\zeta_3$, which are associated with absorbing coefficients, are set to be zeros, those equations yield normal elastic wave equations in the transformed coordinate. Since medium properties are kept the same in the PML as in neighboring computational domain, no reflections will happen at the numerical boundary between the computational domain and the PML. So in the PML, $\zeta_1$, $\zeta_2$ and $\zeta_3$ are set to be zeros at the neighborhood of the numerical boundary and gradually increased toward the outer bound of the PML.

# 4 Staggered-Grid Finite Difference Time-Domain Scheme: A Wavelet Based Formulation and Higher Order Method

By approximating derivatives with differences, the finite difference scheme converts PDEs with linear algebraic equations. The discrepancy between the finite difference solution and the PDE solution consists of

two contributions: the discretization error that causes grid dispersion and anisotropy, and the truncation error due to cutting the infinite long operator into a finite length. Techniques for obtaining a more accurate numerical solution using FDTD has been focused on reducing those two effects, such as using higher-order difference approximations (Dablain, 1986) and staggered grids (Virieux, 1986).

In recent years, there have been several successful applications of wavelet theory to time domain schemes for electrodynamics, based on the method of moments (Harrington, 1993). This method expands wave field components (particle velocities and stresses) to a complete set of orthonormal basis functions, then discretizes the expansion coefficients by taking inner product with a test function which is orthogonal to the basis function. It was shown that the conventional staggered grid FDTD scheme can be derived using the method of moments with pulse functions being the orthonormal basis and test functions Krumpholz and Russer, 1993, 1994). A multiresolution time-domain (MRTD) scheme based on wavelet theory was developed for electrodynamics and exhibits highly linear numerical dispersion characteristics, therefore allowing coarser grid spacing (Krumpholz and Katehi, 1996). In their work, Krumpholz and Katehi employed the Battle-Lemarie scaling and wavelet functions as basis functions. Because those basis functions do not satisfy the interpolation property, the expansion coefficients do not represent direct physical wave field values. Hence it becomes necessary to reconstruct the physical field by taking a weighted sum of neighboring coefficients, resulting in a complicated algorithm and a large computational overhead. In 2001, Fujii and Hoefer avoided the step of reconstruction by using the Deslauriers-Dubuc interpolating functions Dubuc, 1986; Deslauriers and Dubuc, 1989) as the basis functions (Fujii and Hoefer, 2001).

Thus far the wavelet formulation of the FDTD method has not been studied solving elastic wave equations. In this section , we develop a time-domain scheme using a wavelet-based differencing approach Deslauriers-Dubuc interpolating functions to solve the elastic wave equations. The spatial derivative is approximated by Deslauriers-Dubuc interpolating functions and the temporal derivative is approximated by the Harr scaling function (Strang, 1996). The Harr scaling function is a compactly supported step function shown in Figure 4. A comparison of numerical dispersion and accuracy between the wavelet-based scheme and conventional FDTD of order 2, 4, 6 and 8 shows that the wavelet based scheme exhibits similar linear dispersion characteristics as higher order method (6th or 8th order), resulting in a reduction in grid points per wavelength necessary to maintain the same, if not better accuracy than the 4th order scheme. FDTD results from the 1-D wave equation show that wavelet-base formulation produce more accurate reflection and transmission at sharp boundaries.

## 4.1 Interpolating Basis Functions

The Deslauriers-Dubuc interpolating function $\phi$ of order $2p-1$ is the autocorrelation function of the Daubechies compactly supported orthogonal scaling function $\phi_0$ of $p$ vanishing wavelet moments (Mallat, 1997),

$$\phi(x) = \int_{-\infty}^{\infty} \phi_0(u)\phi_0(u-x)du. \tag{24}$$

$\phi$ is compactly supported, has a minimum support of $[-2p+1, 2p-1]$ and is able to reproduce polynomials of order $2p-1$. In addition, being an autocorrelation function, $\phi$ is symmetric. Figures 5 and 6 illustrate Daubechies scaling function and Deslauriers-Dubuc interpolating function. Note that $\phi(x)$ is orthogonal to its integer shift; therefore functions being discretized and expanded to a family of $\phi(x)$ do not require extra computation to be reconstructed. A remarkable property of $\phi$ is that it can be written as a sum of scaled and translated copies of itself. Such a property is called two-scale relation or dilation relation which is denoted as

$$\phi(x) = \sum_{k=-\infty}^{+\infty} h_k^* \phi(2t-k). \tag{25}$$

where coefficients $h_k^*$ is obtained by taking the autocorrelation of Daubechies wavelet filter $h_k$ (Daubechies, 1988). Values of $h_k^*$ for $p$ = 2,4, and 6 are listed in table 4.1. As an initial work, only the scaling functions are chosen as the basis function, therefore $h_k$ is the low-pass decomposition filter of Daubechies wavelet filter family. Results of electrodynamics show that by using only the scaling function itself still lead to savings in the number of grids due to the highly linear dispersion property of the resulting scheme. Incorporating

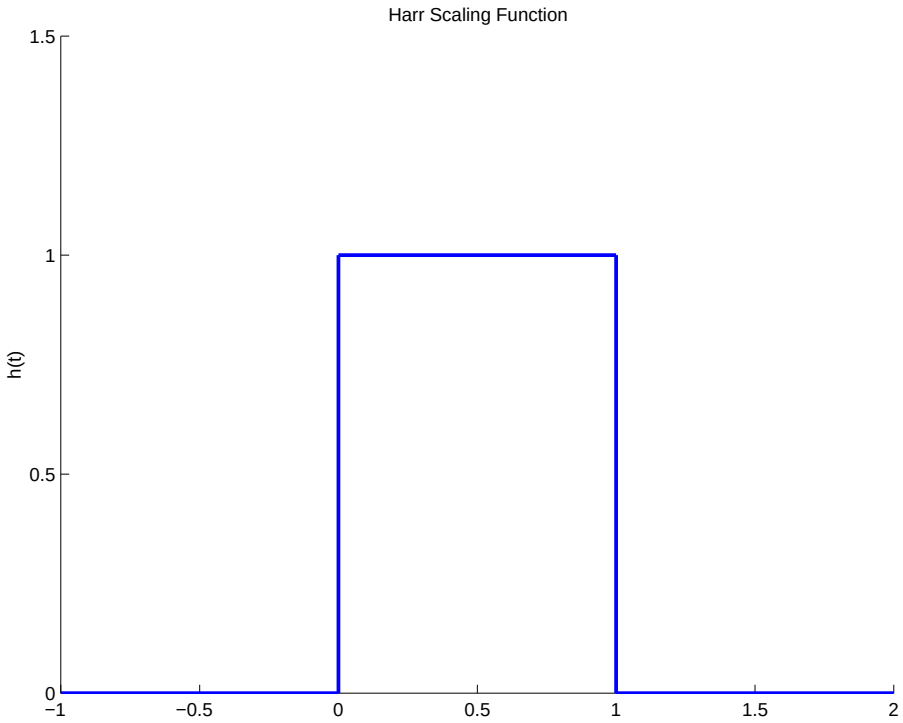


Figure 4: Harr scaling function $h(t)$.

wavelet functions will possibly yield higher resolution schemes. Dirac delta function $\delta(x)$ is chosen to be the dual function of $\phi(x)$, the Deslauriers-Dubuc interpolating function. Denoting the discretization of a function $f(x)$ as

$$f_j(x) = f(\frac{x}{\Delta x} - j) \tag{26}$$

where $f(x)$ represents $\phi(x)$ and its dual function, $\delta(x)$. $\Delta x$ is the grid spacing. Since $f(x)$ is orthogonal to integer shift, $f_j(x)$ is orthogonal to shifts equal to integer times of $\Delta x$. The inner product of $\phi_i(x)$ and $\delta_j(x)$ satisfies the following biorthogonal relation

$$< \phi_i, \delta_j >= \delta_{ij} \tag{27}$$

where $\delta_{ij}$ is the Kronecker delta function. Similar to Deslauriers-Dubuc interpolating function, Harr scaling function is also orthogonal to its integer shift. In order to construct staggered-grid FDTD scheme, Harr scaling function is left shifted by $\frac{1}{2}$ then the corresponding discretization is defined as

$$h_n(t) = h(\frac{t}{\Delta t} - n + \frac{1}{2}) \tag{28}$$

| k | p=2 | p=4 | p=6 |
|---|---|---|---|
| 0 | 1.00000000 | 1.00000000 | 1.00000000 |
| 1 | 0.56250000 | 0.59814453 | 0.61016818 |
| 2 | 0.00000000 | 0.00000000 | 0.00000000 |
| 3 | -0.06250000 | -0.11962891 | -0.14539719 |
| 4 | | 0.00000000 | 0.00000000 |
| 5 | | 0.02392578 | 0.04361916 |
| 6 | | 0.00000000 | 0.00000000 |
| 7 | | -0.00244141 | -0.01038551 |
| 8 | | | 0.00000000 |
| 9 | | | 0.00161552 |
| 10 | | | 0.00000000 |
| 11 | | | -0.00012016 |

Table 1: Filter coefficients $h_k^*$ in equation 25.

| l | p=2 | p=4 |
|---|---|---|
| 0 | 1.2291666667 | 1.3110340773 |
| 1 | -0.0937500000 | -0.1560100710 |
| 2 | 0.0104166667 | 0.0419957460 |
| 3 | | -0.0086543236 |
| 4 | | 0.0008308695 |
| 5 | | 0.0000108999 |
| 6 | | -0.0000000041 |

Table 2: a(l) in equation 32. $a(-l) = -a(l-1)$.

where $\Delta t$ is time step. Similar to $f_j(x)$, $h_n(t)$ is orthogonal to shifts equal to integer times of $\Delta t$. The orthogonality conditions are listed below explicitly.

$$\int_{x=-\infty}^{+\infty} \phi_i(x)\delta_{i'}(x)dx = \delta_{i,i'}\Delta x \tag{29}$$

$$\int_{t=-\infty}^{+\infty} h_n(t)h_{n'}(t)dt = \delta_{n,n'}\Delta t \tag{30}$$

$$\int_{t=-\infty}^{+\infty} \partial_t h_{n+1/2}(t)h_{n'}(t)dt = \delta_{n,n'} - \delta_{n+1,n'} \tag{31}$$

$$\int_{x=-\infty}^{+\infty} \partial_x \phi_{i+1/2}(x)\delta_{i'}(x)dx = \frac{d\phi)x)}{dx}|_{x=i'-i-\frac{1}{2}} \equiv a(l), \quad l = i - i' \tag{32}$$

$a(l)$ in equation 32 is evaluated numerically and are listed in Table 4.1 for $p = 2$ and 4.

## 4.2 Discretization of Elastic Wave Equations

A staggered-grid scheme is employed to discretize the elastic wave equation as it is more stable and accurate. Because spatial derivatives with respect to $x$, $y$ and $z$ in the wave equations are decoupled, illustrating the discretization using Deslauriers-Dubuc interpolating function for a 1-D wave equation will not lose generality. The formulation for the full 3-D wave equation in the stretched coordinated is listed at the end of this subsection.

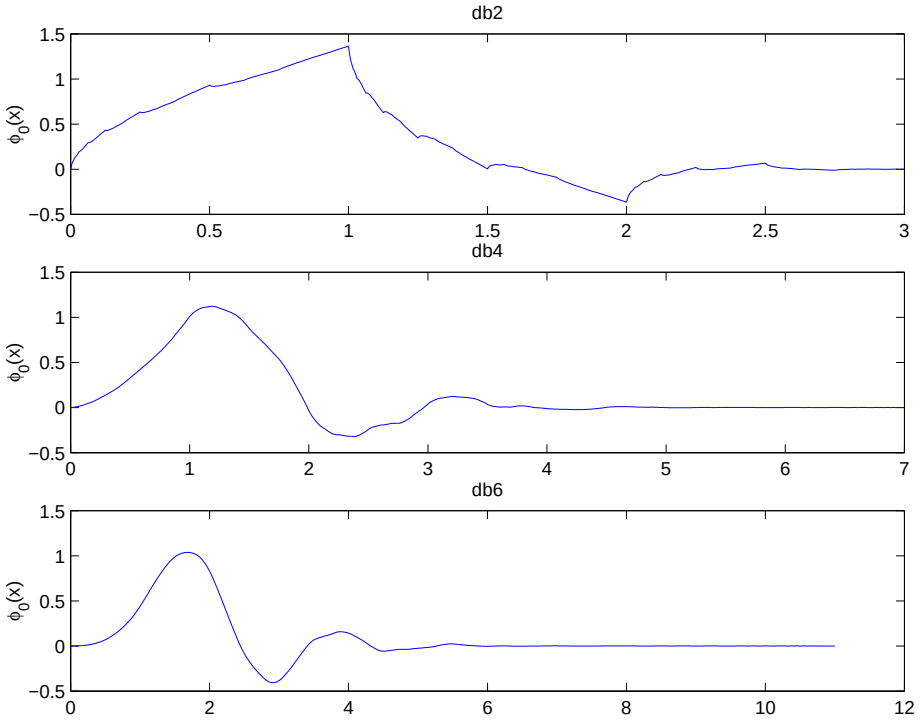


Figure 5: Daubechies compactly supported scaling function $\phi_0$ of 2, 4, and 6 vanishing moments.

### 4.2.1 Discretization of 1-D Wave Equation

The set of 1-D wave equation that needs discretization is

$$\rho(x)\partial_t v_x(x,t) = \partial_x \tau_{xx}(x,t) \tag{33}$$

$$\partial_t \tau_{xx}(x,t) = c_{11}\partial_x v_x(x,t) \tag{34}$$

where the normal stress $\tau_{xx}(x,t)$ and particle velocity $v_x(x,t)$ can be represented by linear combinations of discretized Deslauriers-Dubuc interpolating function $\phi_j(x)$ in space and Harr scaling function $h_n(t)$ in time

$$\tau_{xx}(x,t) = \sum_{i,n=-\infty}^{+\infty} \tau^{xx}_{i+1/2;n}\phi_{i+1/2}(x)h_n(t) \tag{35}$$

$$v(x,t) = \sum_{i,n=-\infty}^{+\infty} v^{x}_{i;n+1/2}\phi_i(x)h_{n+1/2}(t) \tag{36}$$

After substituting equations 35 and 36 to 33, taking inner product of both sides with testing functions $\delta_{i'}(x)$ and $h_{n'}(t)$may yields

$$\begin{aligned}&\int_{x=-\infty}^{+\infty}\int_{t=-\infty}^{+\infty} \partial_t \sum_{i=-\infty}^{+\infty}\sum_{n=-\infty}^{+\infty} \rho_i v^x_{i;n+1/2}\phi_i(x)h_{n+1/2}(t)\delta_{i'}(x)h_{n'}(t)dxdt \\ &= \int_{x=-\infty}^{+\infty}\int_{t=-\infty}^{+\infty} \partial_x \sum_{i=-\infty}^{+\infty}\sum_{n=-\infty}^{+\infty} \tau^{xx}_{i+1/2;n}\phi_{i+1/2}(x)\delta_{i'}(x)h_n(t)h_{n'}(t)dxdt\end{aligned} \tag{37}$$

Applying orthogonality conditions to the above equation leads to the discretization of equation 33

$$v^x_{i';n'+1/2} = v^x_{i';n'-1/2} + \frac{\Delta t}{\rho_{i'}\Delta x}\sum_{l=0}^{Ls-1} a(l)(\tau^{xx}_{i'+\frac{2l-1}{2};n'} - \tau^{xx}_{i'-\frac{2l-1}{2};n'}) \tag{38}$$

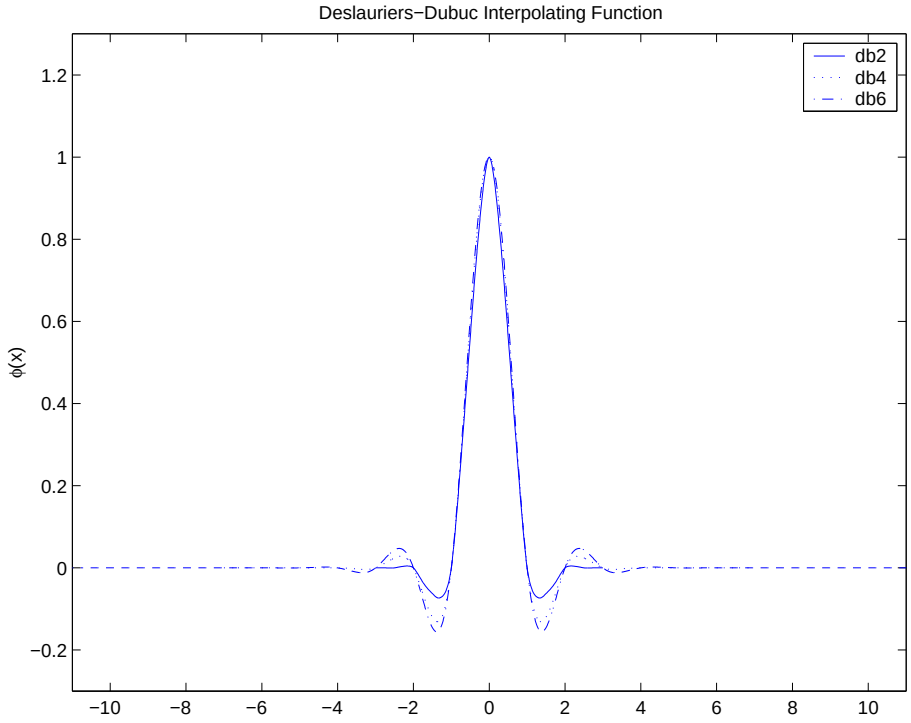


Figure 6: Deslauriers-Dubuc compactly supported interpolating functions of order 3, 7 and 11. They are autocorrelation functions of Daubechies compactly supported scaling function of order 2, 4 and 6, respectively.

where $Ls = 2p-1$, the effective support of the basis function $\phi(x)$. Similarly, equation 34 is then discretized as

$$\tau^{xx}_{i'+1/2;n'+1} = \tau^{xx}_{i'+1/2;n'} + c_{11}^{i'+1/2}\frac{\Delta t}{\Delta x}\sum_{l=0}^{L_s-1} a(l)(v^x_{i'+l;n'+1/2} - v^x_{i'+1-l;n'+1/2}) \tag{39}$$

Until now, the wavelet-based formulation of FDTD for the 1-D wave equation is achieved (equations 38 and 39). To compare with conventional Taylor-expansion based FDTD schemes of 2nd, 4th, 6th and 8th order, the 1-D wave equation is discretized using 2nd, 4th, 6th and 8th order center differencing schemes for spatial derivatives and 2nd order center differencing schemes for temporal derivatives.

$$\begin{aligned} v^x_{i;n+1/2} &= v^x_{i;n-1/2} + \frac{\Delta t}{\Delta x \rho_i}[\eta_1(\tau^{xx}_{i+1/2;n} - \tau^{xx}_{i-1/2;n}) \\ &+ \eta_2(\tau^{xx}_{i+3/2;n} - \tau^{xx}_{i-3/2;n}) \\ &+ \eta_3(\tau^{xx}_{i+5/2;n} - \tau^{xx}_{i-5/2;n}) \\ &+ \eta_4(\tau^{xx}_{i+7/2;n} - \tau^{xx}_{i-7/2;n})] \end{aligned} \tag{40}$$

$$\begin{aligned} \tau^{xx}_{i+1/2;n+1} &= \tau^{xx}_{i+1/2;n} + c_{11}^{i+1/2}\frac{\Delta t}{\Delta x}[\eta_1(v^x_{i+1;n+1/2} - v^x_{i;n+1/2}) \\ &+ \eta_2(v^x_{i+2;n+1/2} - v^x_{i-1;n+1/2}) \\ &+ \eta_3(v^x_{i+3;n+1/2} - v^x_{i-2;n+1/2}) \\ &+ \eta_4(v^x_{i+4;n+1/2} - v^x_{i-3;n+1/2}) \end{aligned} \tag{41}$$

Coefficients $\eta_1$, $\eta_2$, $\eta_3$ and $\eta_4$ are listed in table 4.2.1 for FDTD schemes of order 2, 4, 6 and 8.

| | 2nd order | 4th order | 6th order | 8th order |
|---|---|---|---|---|
| $\eta_1$ | 1 | 9/8 | 75/64 | 1225/1024 |
| $\eta_2$ | | -1/24 | -25/384 | -245/3072 |
| $\eta_3$ | | | 3/640 | 49/5120 |
| $\eta_4$ | | | | -5/7168 |
| discretization error | $O(\Delta x^2)$ | $O(\Delta x^4)$ | $O(\Delta x^6)$ | $O(\Delta x^8)$ |

Table 3: Coefficients of 2nd, 4th, 6th and 8th order finite difference.

#### 4.2.2 Numerical Dispersion and Stability Condition

Like any conventional FDTD scheme, due to the discretization in space and time, the wavelet based FDTD scheme exhibits deviations from the desired linear dispersion behavior. If numerical errors increase over time iteration, the FDTD scheme is not stable. To apply an FDTD algorithm efficiently without losing too much of accuracy, it is important to analyze numerical dispersion and stability condition.

Suppose a plane wave $e^{i(\omega t - kx)}$ is propagating in the medium, it must satisfy the wave equations 33 and 34; that leads to the linear dispersion relation,

$$k^2 = (\frac{\omega}{V_p})^2 \tag{42}$$

where the compressional velocity of the medium $V_p$, equals to $\sqrt{c_{11}/\rho}$. Let $\hat{\omega}$ denotes the numerical angular frequency for a given wave number $k$, and $V_p^{\text{num}}$ denotes the numerical compressional velocity, the ratio of numerical versus true compressional velocity is defined as $q_p$, i.e. $q_p = V_p^{\text{num}}/V_p$. Let $\xi = V_p \frac{\Delta t}{\Delta x}$ and $H = \frac{\Delta x}{\lambda_w}$, where the wavelength $\lambda_w$, equals to $\frac{2\pi}{k}$. $1/H$ represents the number of grid points per wavelength. It shows in the later part of this section that $\xi$ controls the stability, while $H$ controls the numerical dispersion in the FDTD computation. Substituting the plane wave solution which is proportional to $e^{i(\hat{\omega}t - kx)}$ to the difference equations 38 and 39, yields the dispersion relation of the wavelet based FDTD scheme,

$$\frac{1}{\xi} = \frac{\sum_{l=0}^{Ls-1} a(l) \sin(2l+1)\pi H}{\sin \pi H \xi q_p} \tag{43}$$

When $\Delta x \to 0$, $H \to 0$, then $sin(2l+1)\pi H \sim (2l+1)\pi H$ and $sin\pi H \xi q_p \sim \pi H \xi q_p$, equation 43 produces the linear dispersion relation (equation 42) and $V_p^{\text{num}} = V_p$.

Solving for $q_p$, equation 43 yields

$$q_p = \frac{1}{\pi H \xi} \sin^{-1}\{\xi \sum_{l=0}^{L_s-1} a(l) \sin[(2l+1)\pi H]\} \tag{44}$$

The ratio between the real compressional velocity and the numerical one should remain real for a stable FDTD scheme. That requires

$$\xi < \frac{1}{|\sum_{l=0}^{L_s-1} a(l) \sin[(2l+1)\pi H]|} < \frac{1}{\sum_{l=0}^{L_s-1} |a(l)|} = \xi_{\max} \tag{45}$$

Equation 45 is usually called the stability condition. Similarly, applying the plane wave solution to the difference equations 40 and 41 leads to the numerical dispersion relation of conventional FDTD scheme of

the 2nd, 4th, 6th and 8th order.

$$\text{2nd order FDTD: } \frac{1}{\xi} = \frac{\sin \pi H}{\sin \pi H \xi q_p} \tag{46}$$

$$\text{4th order FDTD: } \frac{1}{\xi} = \frac{\eta_1 \sin \pi H + \eta_2 sin 3\pi H}{\sin \pi H \xi q_p} \tag{47}$$

$$\text{6th order FDTD: } \frac{1}{\xi} = \frac{\eta_1 \sin \pi H + \eta_2 \sin 3\pi H + \eta_3 sin 5\pi H}{sin \pi H \xi q_p} \tag{48}$$

$$\text{8th order FDTD: } \frac{1}{\xi} = \frac{\eta_1 \sin \pi H + \eta_2 sin 3\pi H + \eta_3 sin 5\pi H + \eta_4 sin 7\pi H}{\sin \pi H \xi q_p} \tag{49}$$

From the numerical dispersion relations, we may also obtain stability conditions for corresponding conventional FDTD schemes.

$$\xi < \frac{1}{|\eta_1| + |\eta_2| + |\eta_3| + |\eta_4|} = \xi_{\max} \tag{50}$$

where $\eta_1$, $\eta_2$, $\eta_3$ and $\eta_4$ are listed in table 4.2.1.

Figures 8- 14 illustrate numerical errors in the phase velocity produced by wavelet-based and conventional FDTD schemes for various stable time steps $\Delta t$. A general trend shows that for a given accuracy, the wavelet-based FDTD using 7th order Delauriers-Dubuc interpolating function, the autocorrelation function of the 4th order Daubechies scaling function, is more efficient as it requires coarser griding, specifically for coarser time steps ($\xi = \xi_{\max}$, $\xi = 0.8\xi_{\max}$ and $\xi = 0.6\xi_{\max}$).

A 1-D FDTD algorithm that can switch between the 2nd, 4th, 6th, 8th and the wavelet-based schemes is used to test the reflection and transmission at a sharp boundary. The theoretical reflection and transmission coefficients at the sharp boundary should be 1/3 and 2/3, repectively, independent of frequency. Figures 15 and 16 show the transmission coefficients computed from various FDTD algorithms as a function of frequency. Figures 17 and 18 show the reflection coefficients. In all cases, the wavelet-based scheme produce more accurate results. Figure 7 shows the spectrum of the incidence wave for all aforementioned FDTD schems.

### 4.2.3 Discretization of 3-D Wave Equation in Transformed Domain

As the first step to study wave propagations in the LWD situation, we focus our interest on anisotropy and radial heterogeneity. The borehole and its surrounding formation are assumed invariant in the axial(z) direction, and that allows us to Fourier transform the wave equations from the ($x$,$y$,$z$,$t$) domain into the ($x$,$y$,$k_z$,$t$) domain. The finite difference solution of the wave equation is obtained in the ($x$,$y$,$k_z$,$t$) domain and transformed back to the ($x$,$y$,$z$,$t$) domain in the end. The derivative respect to $z$, $\partial_z$, is then replaced by $-ik_z$ (equation 53), instead of using finite difference approximation. Because only $\partial_x$ and $\partial_y$ are computed using finite difference, this type of solution is called 2.5 dimensional solution. As less grid points are needed in the $k_z$ domain than in the $z$ domain, the 2.5D FDTD results a significant reduction in memory requirement. Since solutions for each $k_z$ are independent, efficient parallelization can be achieved trivially. The 3-D wave equations in the transformed domain are discretized in a 2D staggered-grid (Figure 19). To avoid confusion in notations, Fourier transform of z and its inverse transform are explicitly written in equations 51 and 52.

$$\tilde{f}(k_z) = \int_{-\infty}^{+\infty} f(z) e^{ik_z z} dk_z, \tag{51}$$

$$f(z) = \frac{1}{2\pi} \int_{-\infty}^{+\infty} \tilde{f}(k_z) e^{-ik_z z} dz \tag{52}$$

$$\text{Fourier Transform}\{\partial_z f(x,y,z)\} = -ik_z \tilde{f}(x,y,k_z) \tag{53}$$

Similar to the 1-D case, the wave equations are discretized using wavelet-based, 2nd, 4th, 6th and 8th order finite difference. Referring to equations 38, 39, 40 and 41, we define difference operators $D_x \tilde{f}|_{m,j,k}$

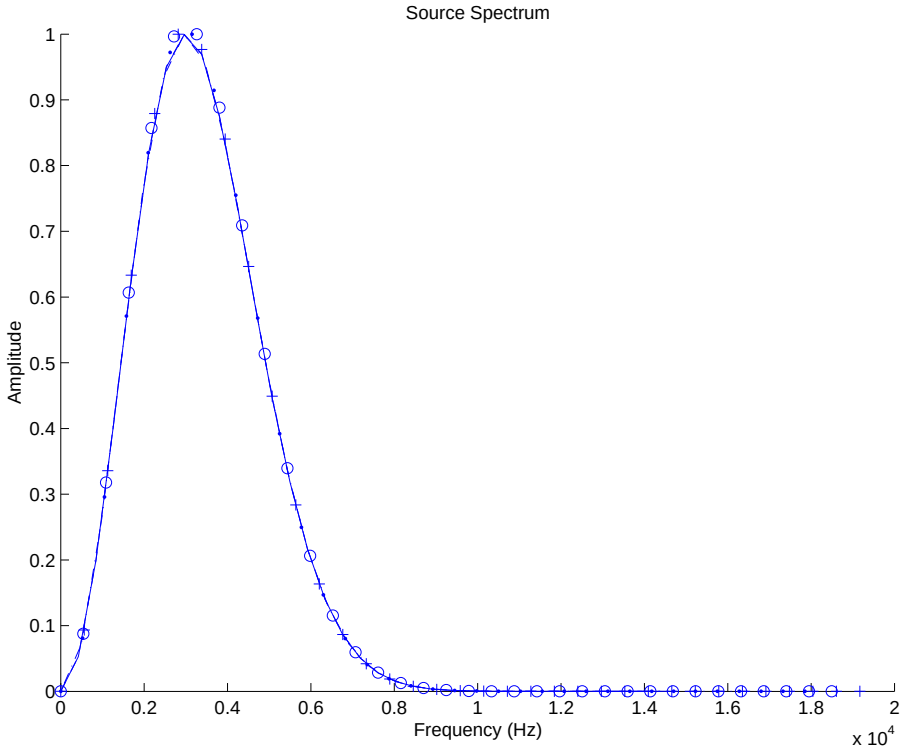


Figure 7: The spectrum of the 1-D incidence wave before it hits the sharp boundary. For all FDTD schemes, 2nd, 4th, 6th, 8th order and the wavelet-based, no numerical dispersion is observed.

and $D_y\tilde{f}|_{m,j,k}$, representing the numerical evaluations at location $(m\Delta x,\ j\Delta y,\ k\Delta k_z)$, of the first order derivatives of $\tilde{f}$ with respect to $x$ and $y$,

$$D_x\tilde{f}|_{m,j,k} = \frac{1}{\Delta x}\sum_{l=0}^{L_s-1} h(l)(\tilde{f}_{m-1/2+l,j,k} - \tilde{f}_{m+1/2-l,j,k}) \tag{54}$$

$$D_y\tilde{f}|_{m,j,k} = \frac{1}{\Delta y}\sum_{l=0}^{L_s-1} h(l)(\tilde{f}_{m,j-1/2+l,k} - \tilde{f}_{m,j+1/2-l,k}) \tag{55}$$

where $h(l) = a(l)$ for wavelet-based finite difference approximation, and for the 2nd, 4th, 6th and 8th order finite difference, $h(0) = 0$, $h(p) = \eta_p$ (for $p = 1, 2, 3, 4$). In the stretching coordinate,

$$D_{\tilde{x}}\tilde{f}|_{m,j,k} = \frac{1}{\epsilon^1(m,:)\Delta\tilde{x}}\sum_{l=0}^{L_s-1} h(l)(\tilde{f}_{m-1/2+l,j,k} - \tilde{f}_{m+1/2-l,j,k}) \tag{56}$$

$$D_{\tilde{y}}\tilde{f}|_{m,j,k} = \frac{1}{\epsilon^2(:,j)\Delta\tilde{y}}\sum_{l=0}^{L_s-1} h(l)(\tilde{f}_{m,j-1/2+l,k} - \tilde{f}_{m,j+1/2-l,k}) \tag{57}$$

where $\epsilon^1(m,:)$ represents discretized $x$ direction stretching function for all possible values of $j$.

Equation 13, the governing equation of the conservation of momentum in both the computational domain and the PML in the transformed coordinate, is Fourier transformed into $k_z$ domain and discretized. When $A = 1$ and $B = 0$, it reduces to the computational domain solution. Let $\Lambda = \rho A$ and $X = \rho B$, discretizing

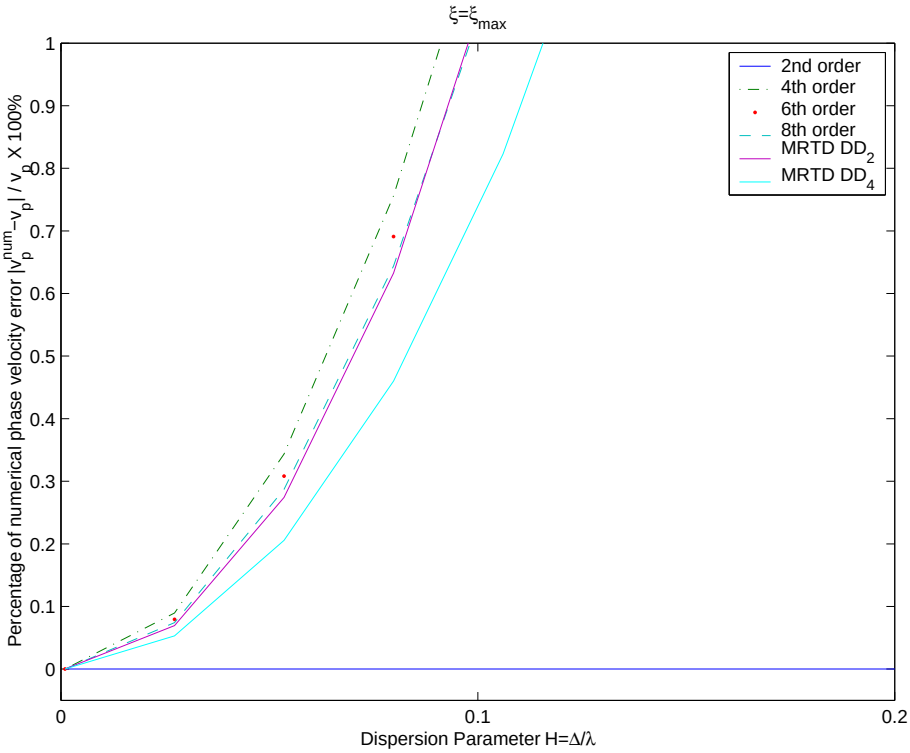


Figure 8: Numerical errors in the phase velocity with respect to $H$. $\Delta t = \xi_{\max}\frac{\Delta x}{V_p}$. Note that for the 2nd order FDTD, $\Delta t = \frac{\Delta x}{V_p}$, which is the so-called magic step relation in which situation the 2nd order FDTD can produce the exact solution for a single phased wave (pure compressional or shear phase) propagating in a homogeneous medium.

the $\tilde{x}$ direction component of equation 13 yields,

$$\begin{aligned} & \Lambda_{m,j+1/2}\frac{\tilde{v}^x_{m,j+1/2,k;n+1/2}-\tilde{v}^x_{m,j+1/2,k;n-1/2}}{\Delta t} + X_{m,j+1/2}\frac{\tilde{v}^x_{m,j+1/2,k;n+1/2}+\tilde{v}^x_{m,j+1/2,k;n-1/2}}{2} \\ = \;& D_{\tilde{x}}\tilde{\tau}^{xx}|_{m,j+1/2,k;n} + D_{\tilde{y}}\tilde{\tau}^{yx}|_{m,j+1/2,k;n} - ik\Delta k_z\tilde{\tau}^{zx}_{m,j+1/2,k;n}\}. \end{aligned} \tag{58}$$

Solving for $\tilde{v}^x_{m,j+1/2,k;n+1/2}$ from equation 58, we obtain the time iteration formula (equation 59) to update $\tilde{v}^x(m\Delta\tilde{x},(j+1/2)\Delta\tilde{y},k\Delta k_z)$, at time step $n+1/2$, i.e. $t=(n+1/2)\Delta t$, from their previous time step values. Similarly, particle velocities , $\tilde{v}^y(m+1/2,j,k)$ and $\tilde{v}^z(m+1/2,j+1/2,k)$ can be updated from their previous time step values by equations 60 and 61, respectively.

$$\begin{aligned} \tilde{v}^x_{m,j+1/2,k;n+1/2} &= \frac{1}{\Psi_{m,j+1/2}}\{(\frac{\Lambda_{m,j+1/2}}{\Delta t}-\frac{X_{m,j+1/2}}{2})\tilde{v}^x_{m,j+1/2,k;n-1/2} \\ &+ D_{\tilde{x}}\tilde{\tau}^{xx}|_{m,j+1/2,k;n} + D_{\tilde{y}}\tilde{\tau}^{yx}|_{m,j+1/2,k;n} \\ &- ik\Delta k_z\tilde{\tau}^{zx}_{m,j+1/2,k;n}\} \end{aligned} \tag{59}$$

$$\begin{aligned} \tilde{v}^y_{m+1/2,j,k;n+1/2} &= \frac{1}{\Psi_{m+1/2,j}}\{(\frac{\Lambda_{m+1/2,j}}{\Delta t}-\frac{X_{m+1/2,j}}{2}))\tilde{v}^y_{m+1/2,j,k;n-1/2} \\ &+ D_{\tilde{x}}\tilde{\tau}^{xy}|_{m+1/2,j,k;n} + D_{\tilde{y}}\tilde{\tau}^{yy}|_{m+1/2,j,k;n} \\ &- ik\Delta k_z\tilde{\tau}^{zy}_{m+1/2,j,k;n} \end{aligned} \tag{60}$$

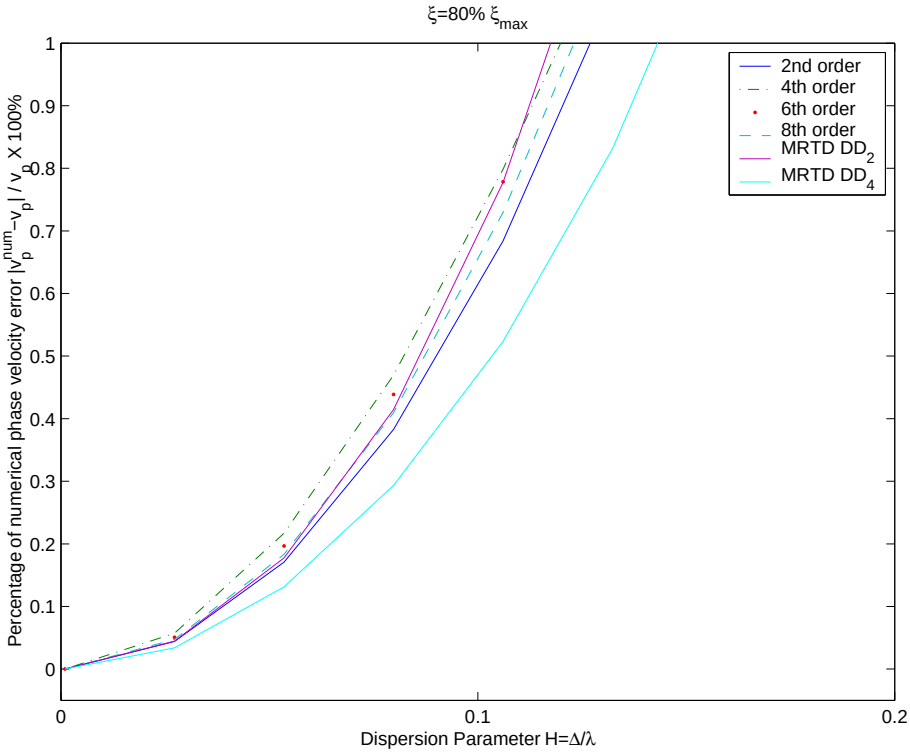


Figure 9: Numerical errors in the phase velocity with respect to $H$. $\Delta t = 0.8\xi_{\max}\frac{\Delta x}{V_p}$.

$$\begin{aligned}\tilde{v}^z_{m+1/2,j+1/2,k;n+1/2} &= \frac{1}{\Psi_{m+1/2,j+1/2}}\{(\frac{\Lambda_{m+1/2,j+1/2}}{\Delta t} - \frac{X_{m+1/2,j+1/2}}{2})\tilde{v}^z_{m+1/2,j+1/2,k;n-1/2} \\ &+ D_{\tilde{x}}\tilde{\tau}^{xz}|_{m+1/2,j+1/2,k;n} + D_{\tilde{y}}\tilde{\tau}^{yz}|_{m+1/2,j+1/2,k;n} \\ &- ik\Delta k_z\tilde{\tau}^{zz}_{m+1/2,j+1/2,k;n} \end{aligned} \tag{61}$$

where

$$\Psi_{m,j} = \frac{\Lambda_{m,j}}{\Delta t} + \frac{X_{m,j}}{2} \tag{62}$$

The constitutive relation of the PML, equations 15 and 21, can reduce to that of the computational domain by simply setting $\zeta_1$, $\zeta_2$ and $\zeta_3$ to zeros. However, the extra tensor $\bar{\bar{E}}^{\mathrm{PML}}$ requires 6 more variables, which is not necessary in the computational domain; therefore, equation 5 is used as the constitutive relation for the computational domain. Discretizing equation 5 in the stretching coordinate leads to the time iteration equations to update each stress component.

$$\begin{aligned}\tilde{\tau}^{xx}_{m+1/2,j+1/2,k;n+1} &= \tilde{\tau}^{xx}_{m+1/2,j+1/2,k;n} \\ &+ \Delta t(d^{11}_{m+1/2,j+1/2}D_{\tilde{x}}\tilde{v}^x|_{m+1/2,j+1/2,k;n+1/2} \\ &+ d^{12}_{m+1/2,j+1/2}D_{\tilde{y}}\tilde{v}^y|_{m+1/2,j+1/2,k;n+1/2} \\ &- d^{13}_{m+1/2,j+1/2}ik\Delta k_z v^z_{m+1/2,j+1/2,k;n+1/2}) \end{aligned} \tag{63}$$

$$\begin{aligned}\tilde{\tau}^{yy}_{m+1/2,j+1/2,k;n+1} &= \tilde{\tau}^{yy}_{m+1/2,j+1/2,k;n} \\ &+ \Delta t(d^{21}_{m+1/2,j+1/2}D_{\tilde{x}}\tilde{v}^x|_{m+1/2,j+1/2,k;n+1/2} \\ &+ d^{22}_{m+1/2,j+1/2}D_{\tilde{y}}\tilde{v}^y|_{m+1/2,j+1/2,k;n+1/2} \\ &- d^{23}_{m+1/2,j+1/2}ik\Delta k_z v^z_{m+1/2,j+1/2,k;n+1/2}) \end{aligned} \tag{64}$$

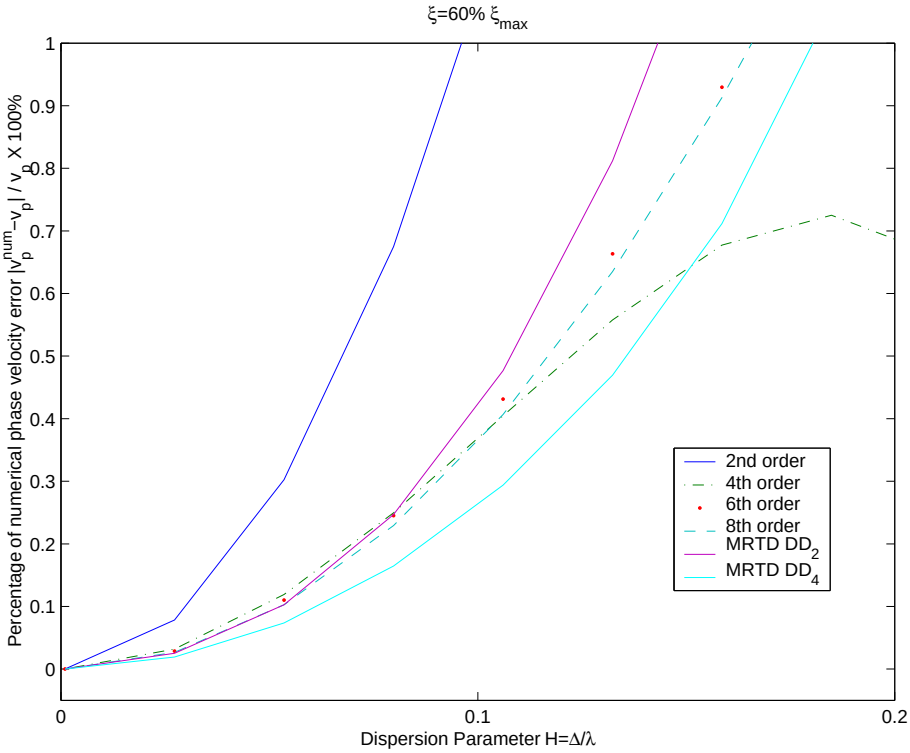


Figure 10: Numerical errors in the phase velocity with respect to $H$. $\Delta t = 0.6\xi_{\max}\frac{\Delta x}{V_p}$.

$$\begin{aligned}
\tilde{\tau}^{zz}_{m+1/2,j+1/2,k;n+1} &= \tilde{\tau}^{zz}_{m+1/2,j+1/2,k;n} \\
&+ \Delta t(d^{31}_{m+1/2,j+1/2} D_{\tilde{x}} \tilde{v}^x|_{m+1/2,j+1/2,k;n+1/2} \\
&+ d^{32}_{m+1/2,j+1/2} D_{\tilde{y}} \tilde{v}^y|_{m+1/2,j+1/2,k;n+1/2} \\
&- d^{33}_{m+1/2,j+1/2} ik\Delta k_z v^z_{m+1/2,j+1/2,k;n+1/2}) \qquad (65)
\end{aligned}$$

$$\begin{aligned}
\tilde{\tau}^{xy}_{m,j,k;n+1} &= \tilde{\tau}^{xy}_{m,j,k;n} \\
&+ \Delta t(d^{41}_{m,j} D_{\tilde{y}} \tilde{v}^x|_{m,j,k;n+1/2} \\
&+ d^{42}_{m+1/2,j+1/2} D_{\tilde{x}} \tilde{v}^y|_{m,j,k;n+1/2}) \qquad (66)
\end{aligned}$$

$$\begin{aligned}
\tilde{\tau}^{yx}_{m,j,k;n+1} &= \tilde{\tau}^{yx}_{m,j,k;n} \\
&+ \Delta t(d^{51}_{m,j} D_{\tilde{y}} \tilde{v}^x|_{m,j,k;n+1/2} \\
&+ d^{52}_{m+1/2,j+1/2} D_{\tilde{x}} \tilde{v}^y|_{m,j,k;n+1/2}) \qquad (67)
\end{aligned}$$

$$\begin{aligned}
\tilde{\tau}^{xz}_{m,j+1/2,k;n+1} &= \tilde{\tau}^{xz}_{m,j+1/2,k;n} \\
&+ \Delta t(-d^{61}_{m,j+1/2} ik\Delta k_z v^x_{m,j+1/2,k;n+1/2} \\
&+ d^{63}_{m,j+1/2} D_{\tilde{x}} \tilde{v}^z|_{m,j+1/2,k;n+1/2}) \qquad (68)
\end{aligned}$$

$$\begin{aligned}
\tilde{\tau}^{zx}_{m,j+1/2,k;n+1} &= \tilde{\tau}^{zx}_{m,j+1/2,k;n} \\
&+ \Delta t(-d^{71}_{m,j+1/2} ik\Delta k_z v^x_{m,j+1/2,k;n+1/2} \\
&+ d^{73}_{m,j+1/2} D_{\tilde{x}} \tilde{v}^z|_{m,j+1/2,k;n+1/2}) \qquad (69)
\end{aligned}$$

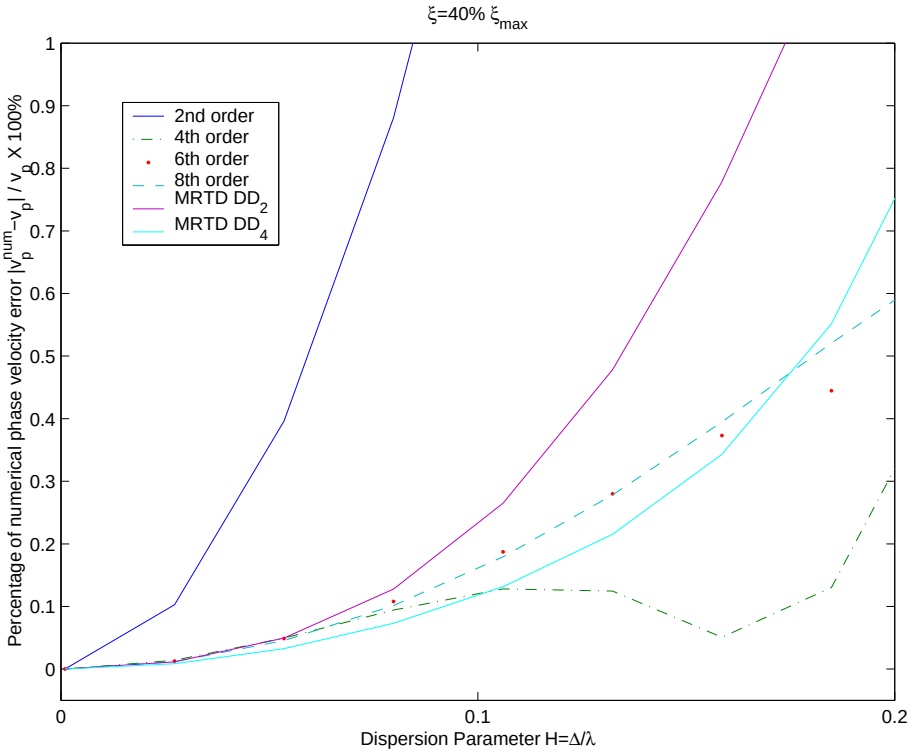


Figure 11: Numerical errors in the phase velocity with respect to $H$. $\Delta t = 0.4\xi_{\max}\frac{\Delta x}{V_p}$.

$$\begin{aligned}\tilde{\tau}^{yz}_{m+1/2,j,k;n+1} &= \tilde{\tau}^{yz}_{m+1/2,j,k;n} \\ &+ \Delta t(-d^{82}_{m+1/2,j} ik\Delta k_z v^{y}_{m+1/2,j,k;n+1/2} \\ &+ d^{83}_{m+1/2,j} D_{\tilde{y}} \tilde{v}^{z}|_{m+1/2,j,k;n+1/2}) \end{aligned} \tag{70}$$

$$\begin{aligned}\tilde{\tau}^{zy}_{m+1/2,j,k;n+1} &= \tilde{\tau}^{zy}_{m+1/2,j,k;n} \\ &+ \Delta t(-d^{92}_{m+1/2,j} ik\Delta k_z v^{y}_{m+1/2,j,k;n+1/2} \\ &+ d^{93}_{m+1/2,j} D_{\tilde{y}} \tilde{v}^{z}|_{m+1/2,j,k;n+1/2}) \end{aligned} \tag{71}$$

When considering wave propagation in an elastic medium without residual stresses, the stress tensor is symmetric, i.e., $\tau_{\alpha\beta} = \tau_{\beta\alpha}$ and $d_{p\alpha}$ denotes the elasticity of the medium. For orthorhombic anisotropy,

$$[d_{p\alpha}] = \begin{bmatrix} c_{11} & c_{12} & c_{13} \\ c_{12} & c_{22} & c_{23} \\ c_{13} & c_{23} & c_{33} \\ c_{66} & c_{66} & 0 \\ c_{66} & c_{66} & 0 \\ c_{55} & 0 & c_{55} \\ c_{55} & 0 & c_{55} \\ 0 & c_{44} & c_{44} \\ 0 & c_{44} & c_{44} \end{bmatrix} \tag{72}$$

Time iteration for stress components in the PML is updated using two steps. First, update the strain rate, $\vec{E}^{\mathrm{PML}}$, from finite difference approximations of the equation 21; then update the stress from difference

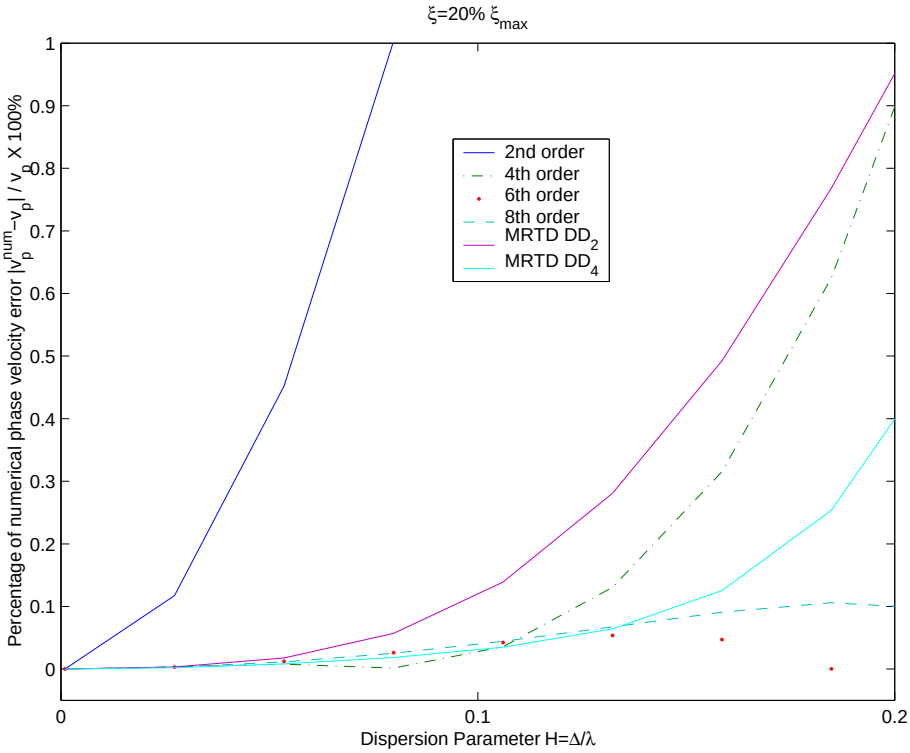


Figure 12: Numerical errors in the phase velocity with respect to $H$. $\Delta t = 0.2\xi_{\max}\frac{\Delta x}{V_p}$.

equations obtained from 15. Before applying finite difference approximations, both equations 21 and 15 are Fourier transformed into ($\tilde{x}$,$\tilde{y}$,$k_z$,t) domain.

$$\tilde{E}^{xx}_{m+1/2,j+1/2,k;n+1} = \frac{1}{\gamma_1^-}(-\gamma_1^+ \tilde{E}^{xx}_{m+1/2,j+1/2,k;n} + D_{\tilde{x}}\tilde{v}^x|_{m+1/2,j+1/2,k;n+1/2}) \tag{73}$$

$$\begin{aligned}\tilde{\tau}^{xx}_{m+1/2,j+1/2,k;n+1} &= \frac{1}{\sigma_1^+}\{\sigma_1^-\tilde{\tau}^{xx}_{m+1/2,j+1/2,k;n} + (d^{11}_{m+1/2,j+1/2}\hat{\tilde{E}}^{xx}_{m+1/2,j+1/2,k;1/2} \\ &+ d^{12}_{m+1/2,j+1/2}\hat{\tilde{E}}^{yy}_{m+1/2,j+1/2,k;1/2} + d^{13}_{m+1/2,j+1/2}\hat{\tilde{E}}^{zz}_{m+1/2,j+1/2,k;1/2})\}\end{aligned} \tag{74}$$

$$\tilde{E}^{yy}_{m+1/2,j+1/2,k;n+1} = \frac{1}{\gamma_2^-}(-\gamma_2^+ \tilde{E}^{yy}_{m+1/2,j+1/2,k;n} + D_{\tilde{y}}\tilde{v}^y|_{m+1/2,j+1/2,k;n+1/2}) \tag{75}$$

$$\begin{aligned}\tilde{\tau}^{yy}_{m+1/2,j+1/2,k;n+1} &= \frac{1}{\sigma_2^+}\{\sigma_2^-\tilde{\tau}^{yy}_{m+1/2,j+1/2,k;n} + (d^{21}_{m+1/2,j+1/2}\hat{\tilde{E}}^{xx}_{m+1/2,j+1/2,k;1/2} \\ &+ d^{22}_{m+1/2,j+1/2}\hat{\tilde{E}}^{yy}_{m+1/2,j+1/2,k;1/2} + d^{23}_{m+1/2,j+1/2}\hat{\tilde{E}}^{zz}_{m+1/2,j+1/2,k;1/2})\}\end{aligned} \tag{76}$$

$$\tilde{E}^{zz}_{m+1/2,j+1/2,k;n+1} = \frac{1}{\gamma_3^-}(-\gamma_3^+ \tilde{E}^{zz}_{m+1/2,j+1/2,k;n} - ik\Delta k_z \tilde{v}^z|_{m+1/2,j+1/2,k;n+1/2}) \tag{77}$$

$$\begin{aligned}\tilde{\tau}^{zz}_{m+1/2,j+1/2,k;n+1} &= \frac{1}{\sigma_3^+}\{\sigma_3^-\tilde{\tau}^{zz}_{m+1/2,j+1/2,k;n} + (d^{31}_{m+1/2,j+1/2}\hat{\tilde{E}}^{xx}_{m+1/2,j+1/2,k;1/2} \\ &+ d^{32}_{m+1/2,j+1/2}\hat{\tilde{E}}^{yy}_{m+1/2,j+1/2,k;1/2} + d^{33}_{m+1/2,j+1/2}\hat{\tilde{E}}^{zz}_{m+1/2,j+1/2,k;1/2})\}\end{aligned} \tag{78}$$

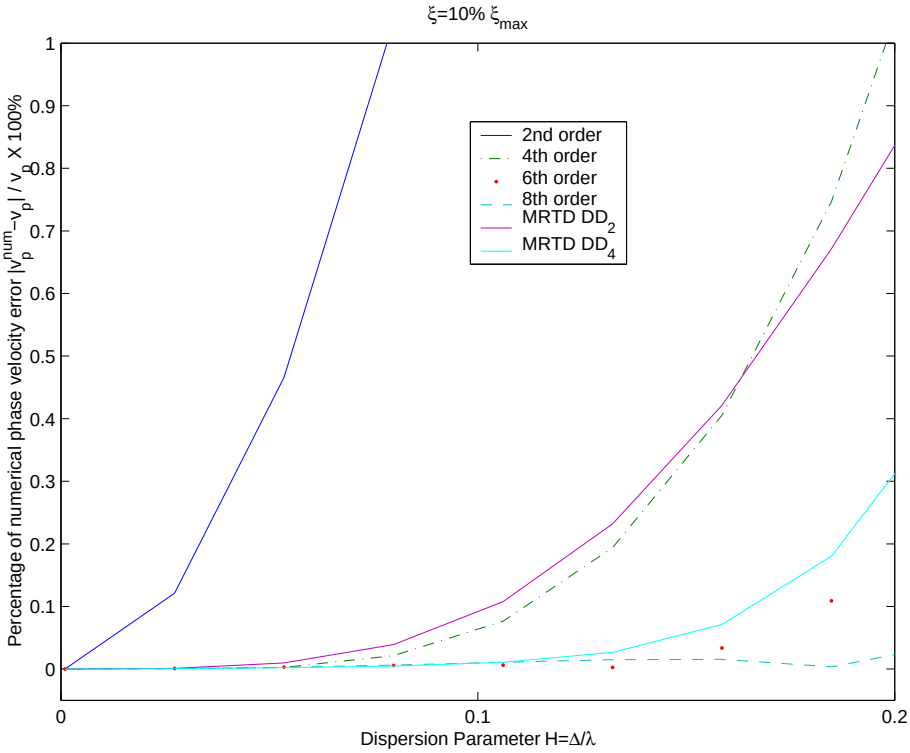


Figure 13: Numerical errors in the phase velocity with respect to $H$. $\Delta t = 0.1\xi_{\max}\frac{\Delta x}{V_p}$.

$$\tilde{E}^{xy}_{m,j,k;n+1} = \frac{1}{\gamma_1^-}(-\gamma_1^+ \tilde{E}^{xy}_{m,j,k;n} + D_{\tilde{x}}\tilde{v}^y|_{m,j,k;n+1/2}) \tag{79}$$

$$\tilde{E}^{yx}_{m,j,k;n+1} = \frac{1}{\gamma_2^-}(-\gamma_2^+ \tilde{E}^{yx}_{m,j,k;n} + D_{\tilde{y}}\tilde{v}^x|_{m,j,k;n+1/2}) \tag{80}$$

$$\begin{aligned}\tilde{\tau}^{xx}_{m,j,k;n+1} &= \frac{1}{\sigma_1^+}\{\sigma_1^-\tilde{\tau}^{xy}_{m,j,k;n} + d^{41}_{m,j}\hat{\tilde{E}}^{yx}_{m,j,k;1/2} \\ &+ d^{42}_{m,j}\hat{\tilde{E}}^{xy}_{m,j,k;1/2}\}\end{aligned} \tag{81}$$

$$\begin{aligned}\tilde{\tau}^{yx}_{m,j,k;n+1} &= \frac{1}{\sigma_2^+}\{\sigma_2^-\tilde{\tau}^{yx}_{m,j,k;n} + d^{51}_{m,j}\hat{\tilde{E}}^{yx}_{m,j,k;1/2} \\ &+ d^{52}_{m,j}\hat{\tilde{E}}^{xy}_{m,j,k;1/2}\}\end{aligned} \tag{82}$$

$$\tilde{E}^{xz}_{m,j+1/2,k;n+1} = \frac{1}{\gamma_1^-}(-\gamma_1^+ \tilde{E}^{xz}_{m,j+1/2,k;n} + D_{\tilde{x}}\tilde{v}^z|_{m,j+1/2,k;n+1/2}) \tag{83}$$

$$\tilde{E}^{zx}_{m,j+1/2,k;n+1} = \frac{1}{\gamma_3^-}(-\gamma_3^+ \tilde{E}^{zx}_{m,j+1/2,k;n} - ik\Delta k_z\tilde{v}^x|_{m,j+1/2,k;n+1/2}) \tag{84}$$

$$\begin{aligned}\tilde{\tau}^{xz}_{m,j+1/2,k;n+1} &= \frac{1}{\sigma_1^+}\{\sigma_1^-\tilde{\tau}^{xz}_{m,j+1/2,k;n} + d^{61}_{m,j}\hat{\tilde{E}}^{zx}_{m,j+1/2,k;1/2} \\ &+ d^{63}_{m,j}\hat{\tilde{E}}^{xz}_{m,j+1/2,k;1/2}\}\end{aligned} \tag{85}$$

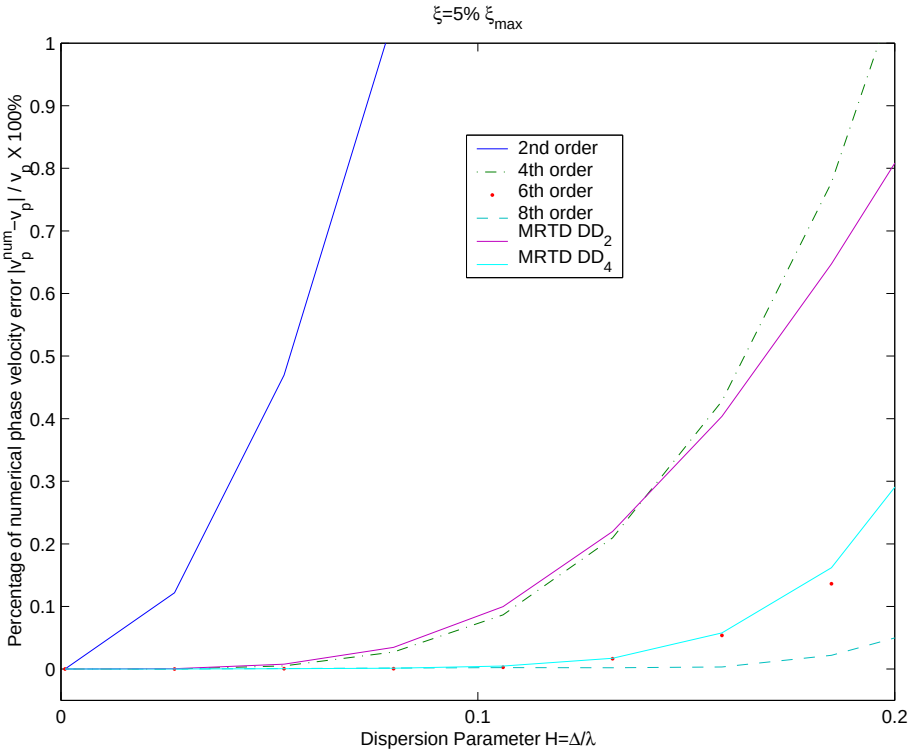


Figure 14: Numerical errors in the phase velocity with respect to $H$. $\Delta t = 0.05\xi_{\max}\frac{\Delta x}{V_p}$.

$$\begin{aligned}\tilde{\tau}^{zx}_{m,j+1/2,k;n+1} &= \frac{1}{\sigma_3^+}\{\sigma_3^-\tilde{\tau}^{zx}_{m,j+1/2,k;n} + d^{71}_{m,j}\hat{\tilde{E}}^{zx}_{m,j+1/2,k;1/2} \\ &+ d^{73}_{m,j}\hat{\tilde{E}}^{xz}_{m,j+1/2,k;1/2}\} \end{aligned} \tag{86}$$

$$\tilde{E}^{yz}_{m+1/2,j,k;n+1} = \frac{1}{\gamma_2^-}(-\gamma_2^+\tilde{E}^{yz}_{m+1/2,j,k;n} + D_{\tilde{y}}\tilde{v}^z|_{m+1/2,j,k;n+1/2}) \tag{87}$$

$$\tilde{E}^{zy}_{m+1/2,j,k;n+1} = \frac{1}{\gamma_3^-}(-\gamma_3^+\tilde{E}^{zy}_{m+1/2,j,k;n} - ik\Delta k_z\tilde{v}^y|_{m+1/2,j,k;n+1/2}) \tag{88}$$

$$\begin{aligned}\tilde{\tau}^{yz}_{m+1/2,j,k;n+1} &= \frac{1}{\sigma_2^+}\{\sigma_2^-\tilde{\tau}^{yz}_{m+1/2,j,k;n} + d^{82}_{m+1/2,j}\hat{\tilde{E}}^{zy}_{m+1/2,j,k;1/2} \\ &+ d^{83}_{m+1/2,j}\hat{\tilde{E}}^{yz}_{m+1/2,j,k;1/2}\} \end{aligned} \tag{89}$$

$$\begin{aligned}\tilde{\tau}^{zy}_{m+1/2,j,k;n+1} &= \frac{1}{\sigma_3^+}\{\sigma_3^-\tilde{\tau}^{zy}_{m+1/2,j,k;n} + d^{92}_{m+1/2,j}\hat{\tilde{E}}^{zy}_{m+1/2,j,k;1/2} \\ &+ d^{93}_{m+1/2,j}\hat{\tilde{E}}^{yz}_{m+1/2,j,k;1/2}\} \end{aligned} \tag{90}$$

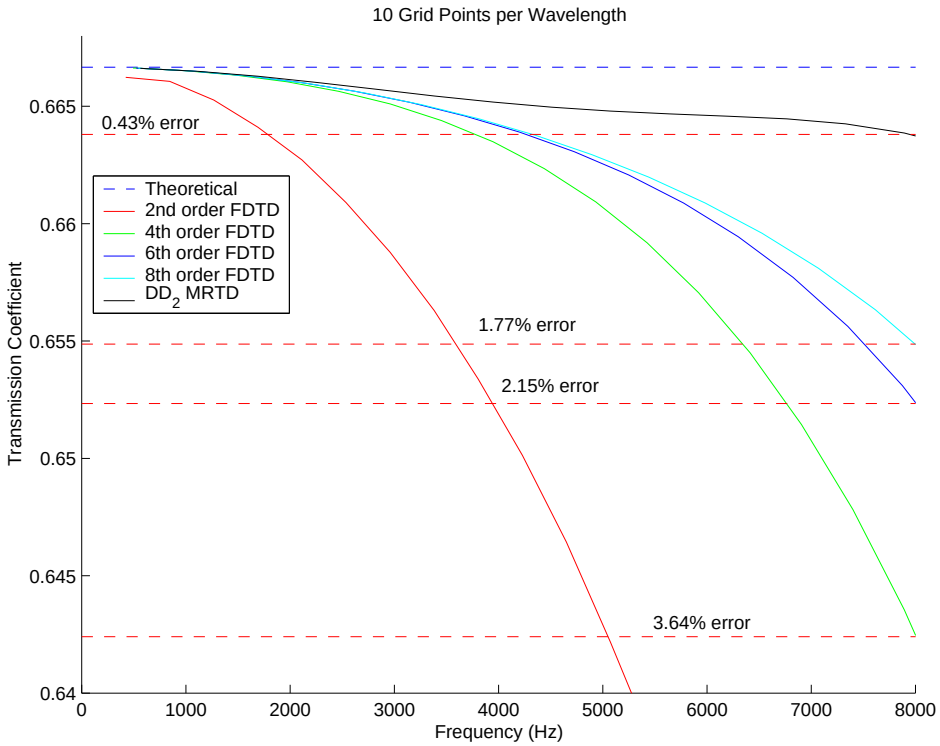


Figure 15: Transmission coefficients obtained from FDTD computations. The wavelet-based FDTD outperforms conventional FDTDs.

where

$$\gamma_p^+ = \frac{\zeta_p}{\omega\Delta t} + \frac{1}{2} \tag{91}$$

$$\gamma_p^- = -\frac{\zeta_p}{\omega\Delta t} + \frac{1}{2} \tag{92}$$

$$\sigma_p^+ = \frac{R\pi^p}{\Delta t} + \frac{I\pi^p}{2} \tag{93}$$

$$\sigma_p^- = \frac{R\pi^p}{\Delta t} - \frac{I\pi^p}{2} \tag{94}$$

with $p = 1$, 2 and 3. $\hat{\tilde{E}}^{\alpha\beta}_{m,j,k;n+1/2}$ represents the average of the strain rate component at current and previous time steps, i.e.

$$\hat{\tilde{E}}^{\alpha\beta}_{m,j,k;n+1/2} = \frac{\tilde{E}^{\alpha\beta}_{m,j,k;n+1} + \tilde{E}^{\alpha\beta}_{m,j,k;n}}{2} \tag{95}$$

At this point, we have established finite difference solutions for the elastic wave equations in the computational domain and the PML. Because all equations are derived in the stretching coordinate, depending on the shape of stretching functions $\epsilon^1(\tilde{x})$ and $\epsilon^1(\tilde{x})$, grid size in the physical domain is variable. Following the same approach as for the 1-D case, we may obtain the stability condition for the 2.5D FDTD scheme,

$$\xi \leq \frac{1}{\sum_{l=0}^{L_s-1}|h(l)|}(2 + \frac{k_z^2\Delta^2}{4})^{-\frac{1}{2}} \tag{96}$$

For simplicity, let $\Delta x = \Delta y = \Delta$.

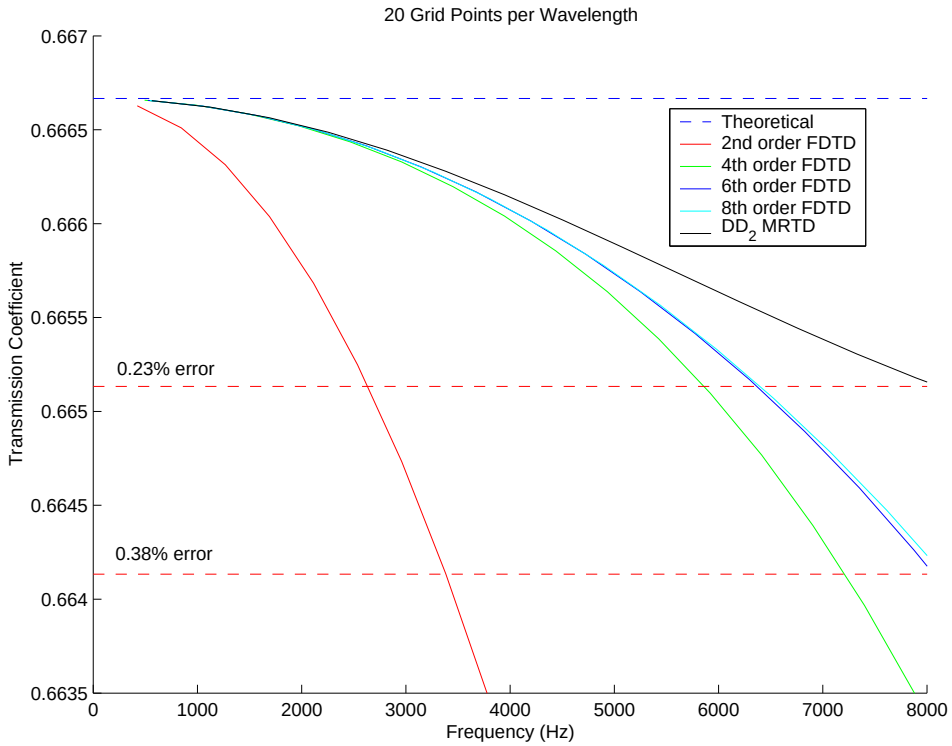


Figure 16: Transmission coefficients obtained from FDTD computations. The wavelet-based FDTD outperforms conventional FDTDs.

# 5 Test of Finite Difference Method

We implemented a staggered-grid 2.5D FDTD code with the anisotropic PML using 2nd order center difference for temporal derivatives. For spatial derivatives, we leave the option to the user, depending on their specific needs, of selecting 2nd, 4th, 6th, 8th and wavelet-based difference schemes. The program can take an arbitrary heterogeneous model. The grid size can be non-uniform and the user can specify where and how the grid should be stretched. The Kelly wavelet is employed as the source function (Stephen et al., 1985).

First, we test our algorithm with a point source in a homogeneous acoustic medium, and compare the results with Green's function solution. Then, we test it with a point source in a fluid-filled borehole.

## 5.1 Homogeneous Acoustic Medium

By setting the shear velocity at zero, we obtain an acoustic medium. The point source solution to the wave equation in a homogeneous acoustic medium is proportional to $g(t - r/V_p)/r$, where $g(t)$ is the Kelly source function, $r$ is the source-receiver distance.

The variable grid option is turned off. Wavelet-based(DD4) difference is chosen to approximate spatial derivatives. We choose 500 Hz as the center frequency, the compressional velocity as 3000 m/s and the density as 2000 kg/m$^3$. The grid size is 0.5 m, implying 12 grid points per wavelength. $k_z$ was chosen from 0 to 6.28 1/m with a spacing of 0.0314 1/m. The source and receiver layout is shown in Figures 20 and 22. Both analytical (Green's function solution) and the FDTD results are shown in Figure 21 and 23. The FDTD results agree with the analytical solution very well.

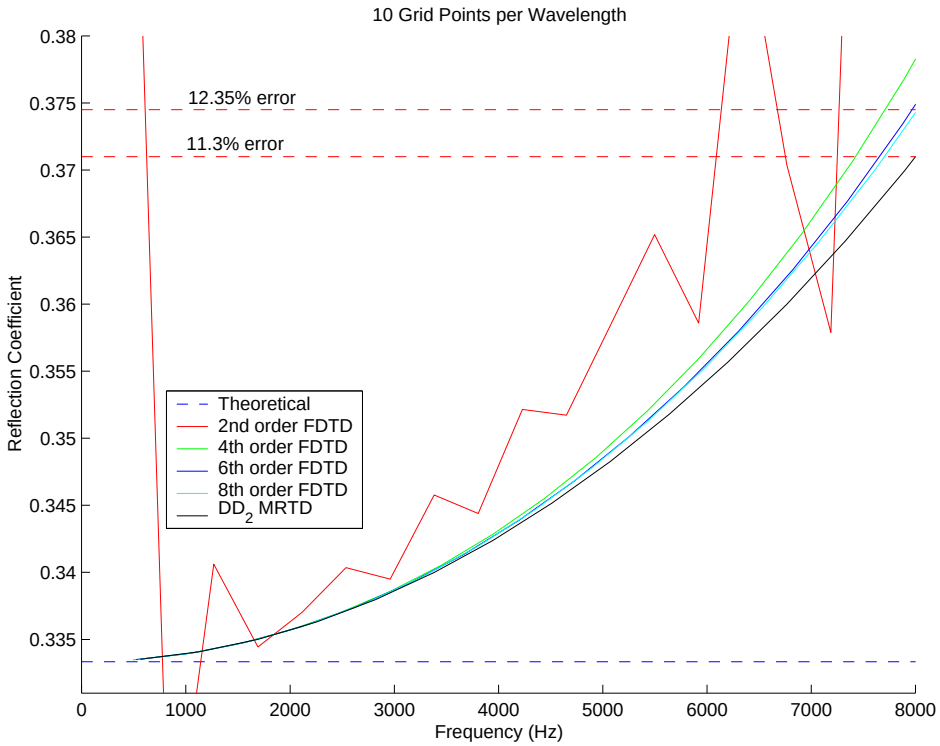


Figure 17: Reflection coefficients obtained from FDTD computations. The wavelet-based FDTD outperforms conventional FDTDs.

## 5.2 Fluid-filled Borehole With Monopole Source

We test our new algorithm with the classic acoustic logging model: a fluid-filled borehole with a monopole source at the center, as the main purpose of developing the new FDTD algorithm in this paper is to study wave propagation in a borehole.Wave propagation in a fluid-filled borehole has been well studied analytically (Biot, 1952). Physical properties of the fluid and formation are listed in table 5.2. Shown in Figure 24, the mesh is finer inside borehole and coarser in the formation. The stretching function $\epsilon^1(\tilde{x}) = \epsilon^2(\tilde{y})$, is illustrated in Figure 26. A top view of the discretized borehole is shown in Figure 25. If using same grid numbers, a uniform grid would discretize the borehole less smooth and circular. Figure 27 shows the top view of the borehole discretized by a uniform grid. The source center frequency is chosen as 8 Khz. $k_z$ is chosen from 0 to 180.5 1/m with $\Delta k_z$ equal to 0.5 1/m. 8th order differencing scheme is chosen to approximate spatial derivatives. The finest grid size is 0.007 m, from the center of the borehole to a radial length of 0.15 m. The coarsest grid size is 0.021 m. The transition zone between the fine and the coarse grid is 0.1 m.

The total grid size is $112 \times 112 \times 362$. As results in $k_z$ domain are independent, it is trivial to divide the model into several pieces with each piece running on one machine if a single machine does not have enough memory to hold the whole model. It took three 1.4 GHz Pentium PC 19 hours to complete the simulation.

Figure 28 shows the waveforms received from the eight receivers. The waveforms are then subjected to the dispersion analysis, an algorithm developed at ERL (Nolte et al., 1997). The results are plotted against the theoretical curves 29. The numerical results clearly show the Stoneley mode and the first order pseudo-Rayleigh mode, agreeing with the analytical solution very well. Further semblance analysis result also clearly shows those two modal arrivals as well as the compressional arrival 30.

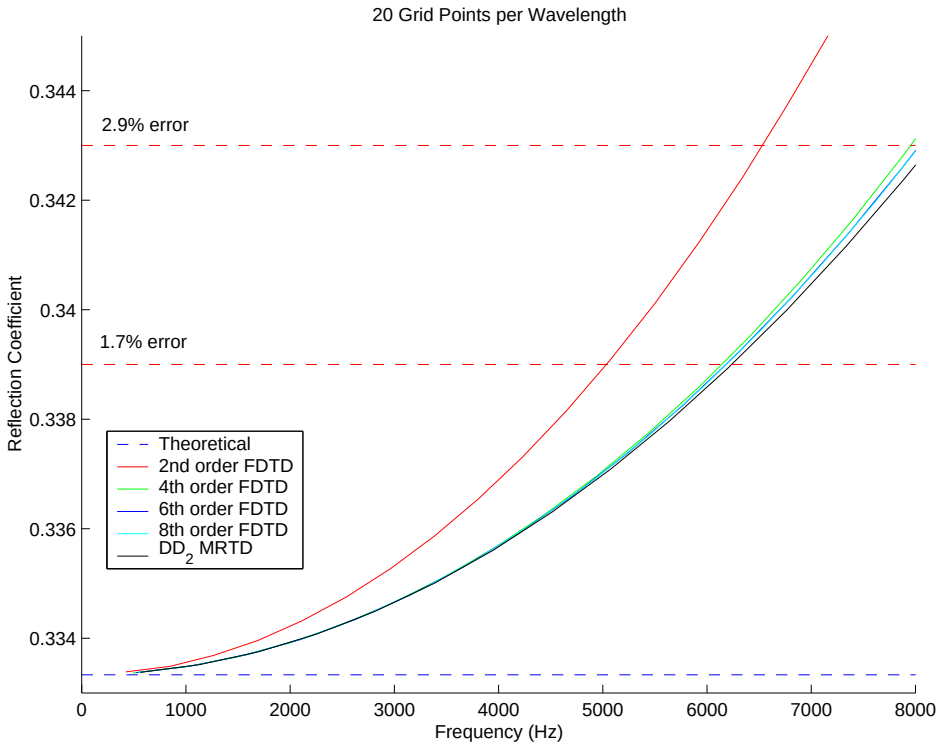


Figure 18: Reflection coefficients obtained from FDTD computations. The wavelet-based FDTD outperforms conventional FDTDs.

# 6 Conclusions

We investigated the efficiency and accuracy of the finite difference time domain scheme from three prospectives: the griding scheme, the differencing operator, and the numerical truncation scheme. A coordinate stretching approach was developed to discretize the physical space using variable grid size. Testing with a borehole model, we proved that this is stable, easy to implement, and most of all efficient and accurate. For the differencing operator, we formulated a wavelet-based differencing scheme, which exhibits linear properties, thus allowing for coarser griding. Besides improved efficiency, the wavelet-based FDTD is more accurate for reflections and transmissions at a sharp boundary. We also formulated the popular anisotropic PML in the stretching coordinate.

# 7 Acknowledgments

This work was supported by the M.I.T. Borehole Acoustics and Logging Consortium, and by the Founding Members of the Earth Resources Laboratory at the Massachusetts Institute of Technology.

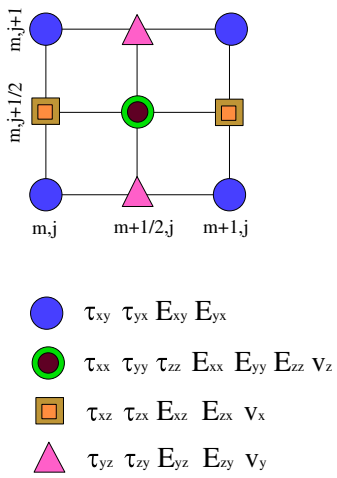


Figure 19: Schematics of staggered-grids for 2.5D schemes.

| | | |
|---|---|---|
| water | $\rho$<br>$V_p$ | 1000<br>1500 |
| formation | $\rho$<br>$V_p$<br>$V_s$ | 2000<br>3000<br>2000 |
| borehole radius | r | 0.1 |
| source 1st receiver offset | $z_0$ | 3.3528 |
| receiver offset | dz | 0.1524 |
| number of receivers | nrec | 8 |

Table 4: Model parameters.

# References


Alterman, Z. and Karal, F. C. (1968). Propagation of elastic waves in layered media by finite difference methods. *Bulletin of the Seismological Society of America*, 58:367–398.

Berenger, J. P. (1994). A perfectly matched layer for the absorption of electromagnetic-waves. *J. Comput. Phys.*, 114:185–200.

Biot, M. (1952). Propagation of elastic waves in a cylindrical bore containing a fluid. *J. Appl. Phys.*, 23:997.

Browning, G., Kreiss, H. O., and Oliger, J. (1973). Mesh refinement. *Mathematics of Computation*, 27:29–39.

Cerveny, V. (2001). *Seismic Ray Theory*. Cambridge University Press.

Chen, K. (1984). Numerical modeling of elasic wave propagation in anisotropic inhomogeneous media: a finite element approach. *Ann. Internat. Msg. of soc. Expl. Geophys., Expanded Abstracts*, pages 631–632.

Crowder, H. J. and Dalton, C. (1971). Erros in the use of nonuniform mesh systems. *Journal of Computational Physics*, 7:32–45.

Dablain, M. A. (1986). The application of high-order differencing to the scalar wave equation. *Geophysics*, 51:54–66.

Daubechies, I. (1988). Orthogonal bases of compactly supported wavelets. *Commun. Pure and Appl. Math*, 41:909–996.

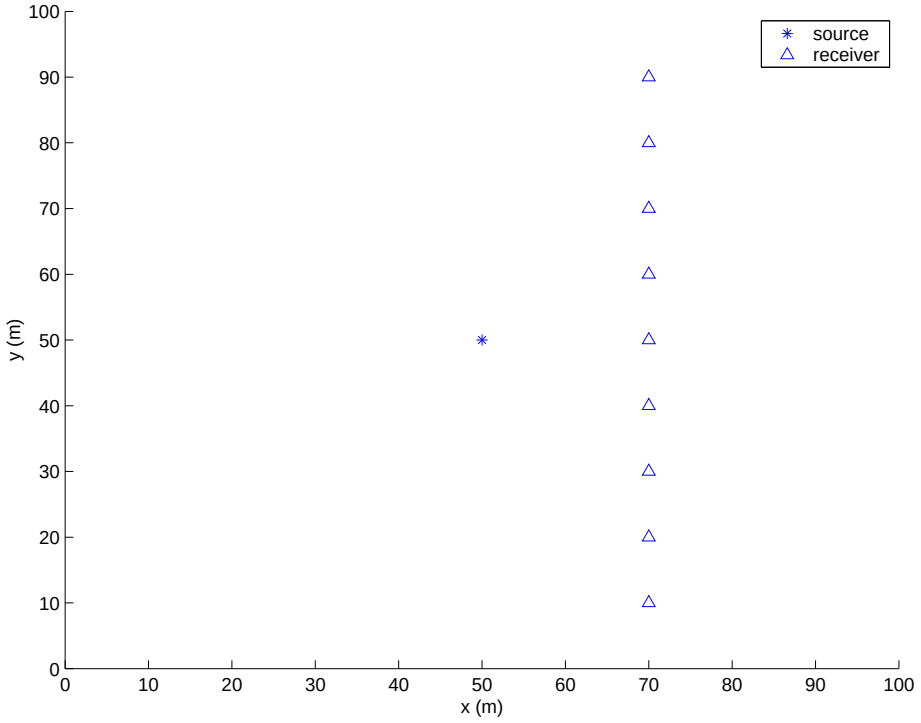


Figure 20: The source and receivers layout for traces in Figure 21. The receivers are lined up in the y direction.

Emmerich, H. (1992). Psv-wave propagation in a medium with local heterogeneities: a hybrid formulation and its application. *Geophysical Journal International*, 109:54–64.

Fujii, M. and Hoefer, W. J. (2001). A wavelet formulation of the finite-difference method: Full-vector analysis of optical waveguid junctions. *IEEE Journal of Quantum Electronics*, 37(8):1015–1029.

Harrington, R. F. (1993). *Field computation by moment methods*. IEEE Press series on electromagnetic waves. Piscataway, NJ : IEEE Press.

Kalnay de Rivas, E. (1972). On the use of non-uniform grids in finite-fifference equations. *Journal of Computational Physics*, 10:202–210.

Kelly, K. R., Ward, R. W., Treitel, S., and Alford, R. M. (1976). Synthetic seismograms: A finite-difference approach. *Geophysics*, 41:2–27.

Kosloff, D. and Baysal, E. (1982). Forward Modeling by a Fourier Method. *Geophysics*, 47:1402–1412.

Krumpholz, M. and Katehi, L. P. B. (1996). Mrtd: New time-domain schemes based on multiresolution analysis. *IEEE Transactions on Microwave Theory and Techniques*, 44(4):555–571.

Levander, A. R. (1988). Fourth-order finite-difference p-sv seismograms. *Geophysics*, 53:1425–1436.

Liu, Q. H. (1999). Perfectly matched layers for elastic waves in cylindrical and spherical coordinates. *J. Acoust. Soc. Am.*, 105:2075–2084.

Mallat, S. G. (1997). *A Wavelet Tour of Signal Processing*. San Diego, CA:Academic.

Muller, G. (1985). The reflectivity method: a tutorial. *Geophysics*, 58:153–174.

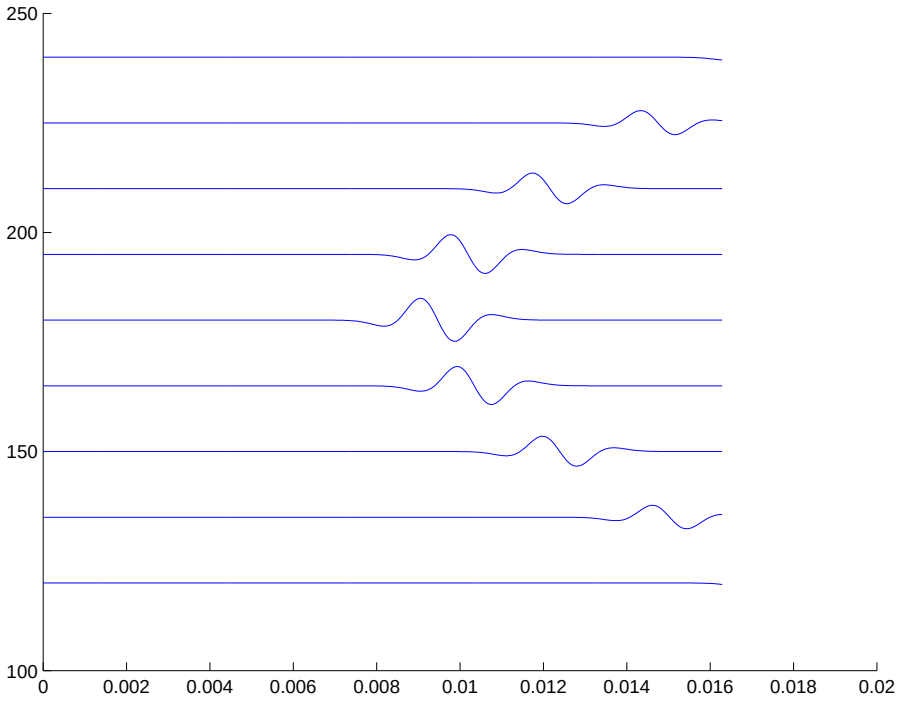


Figure 21: FDTD results (DD4 is used) agree with Green's function results perfectly. The source and receivers setup is shown in Figure 20.

Nolte, B., Rao, R., and Huang, X. (1997). Dispersion analysis of split flexural waves. *Borehole Acoustics and Logging/Reservoir Delineation Consortia Annual Report, MIT*.

Stephen, R. A., Cardo-Casas, F., and Cheng, C. (1985). Finite-difference synthetic acoustic logs. *Geophysics*, 50:1588–1609.

Strang, G. (1996). *Wavelets and Filter Banks*. Wellesley-Cambridge Press.

Taflove, A. (1998). *Advances in Computational Electrodynamics: The Finite-Difference Time-Domain Method*, chapter 1. Artech House.

Virieux, J. (1986). P-sv wave propagation in heterogeneous media: Velocity-stress finite difference method. *Geophysics*, 51:345–369.

Zheng, Y. and Huang, X. (2001). Anisotropic perfectly matched layers for elastic waves in cartesian and curvilinear coordinate. to be revised for submission.

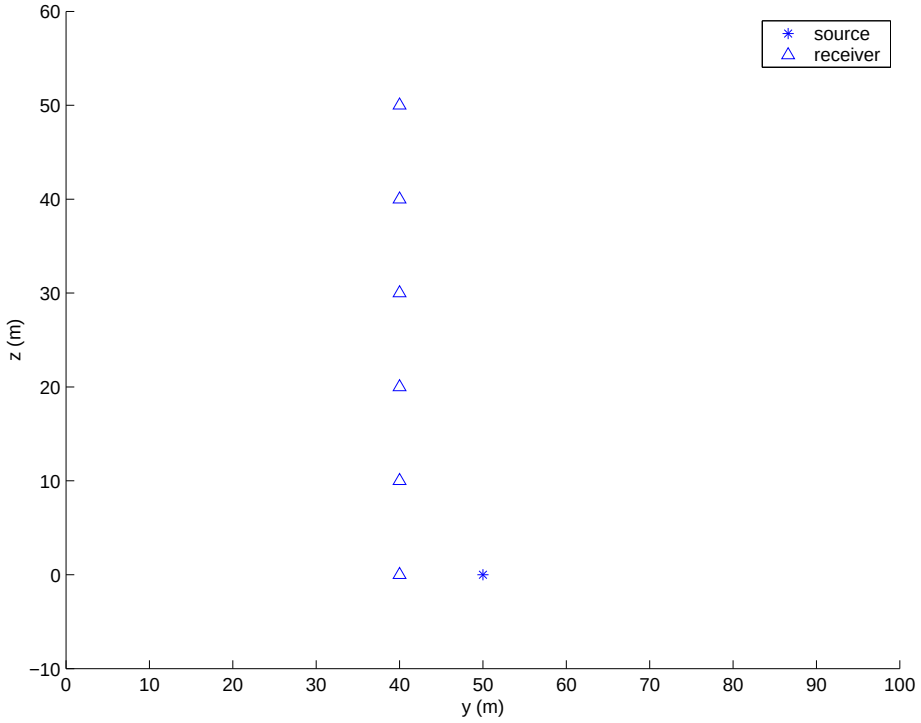


Figure 22: The source and receivers layout for traces in Figure 23. The receivers are lined up in the z direction.

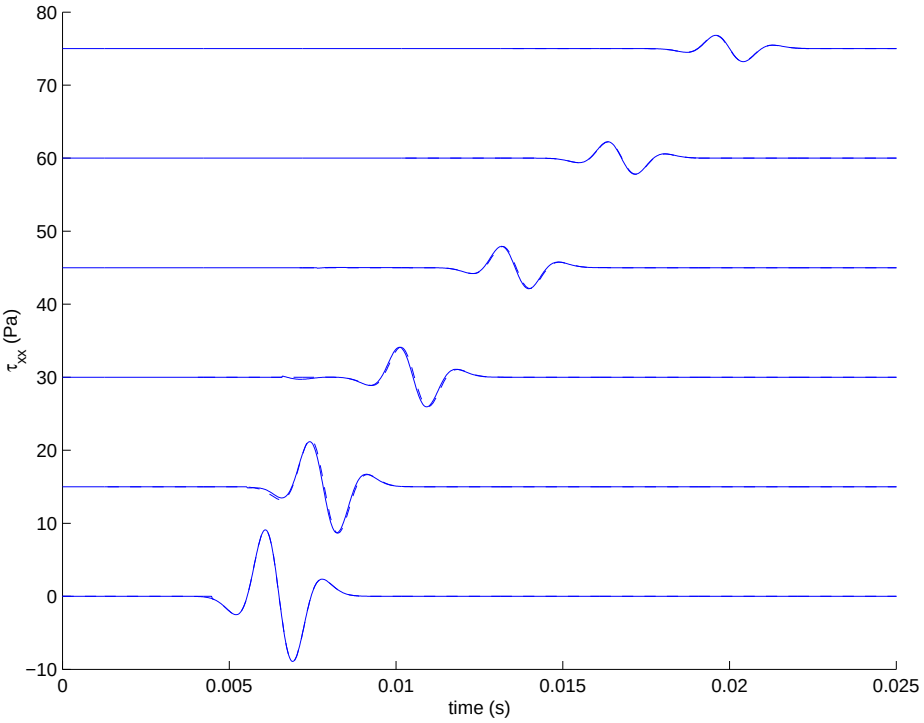


Figure 23: FDTD results (DD4 is used) agree with Green's function results very well. The source and receivers setup is shown in Figure 22.

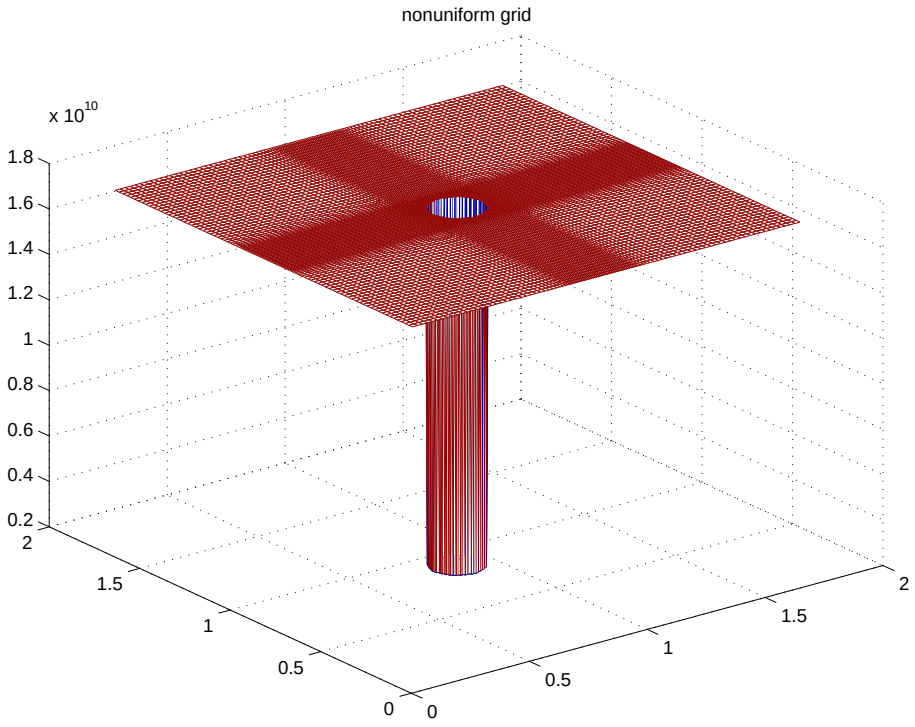


Figure 24: Grid mesh of the fluid-filled borehole model. The mesh is finer inside borehole and coarser in the formation.

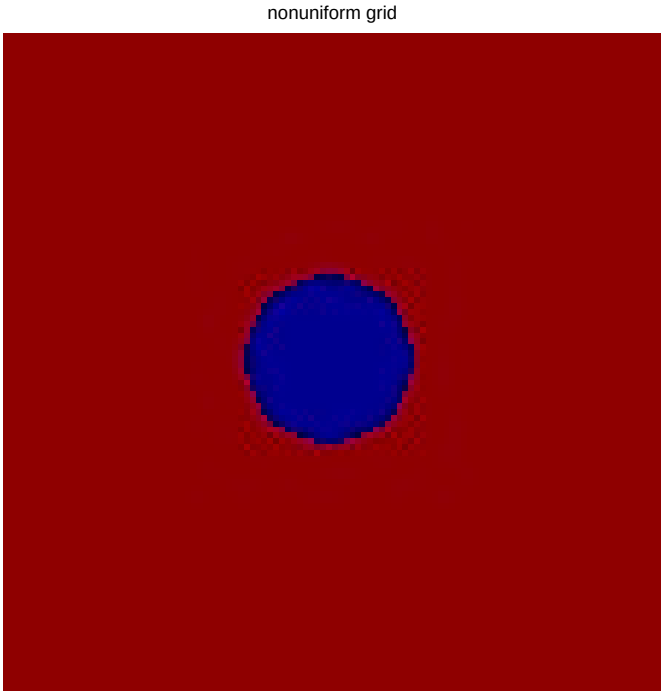


Figure 25: The top view of the discretized borehole using stretching grids shown in Figure 24.

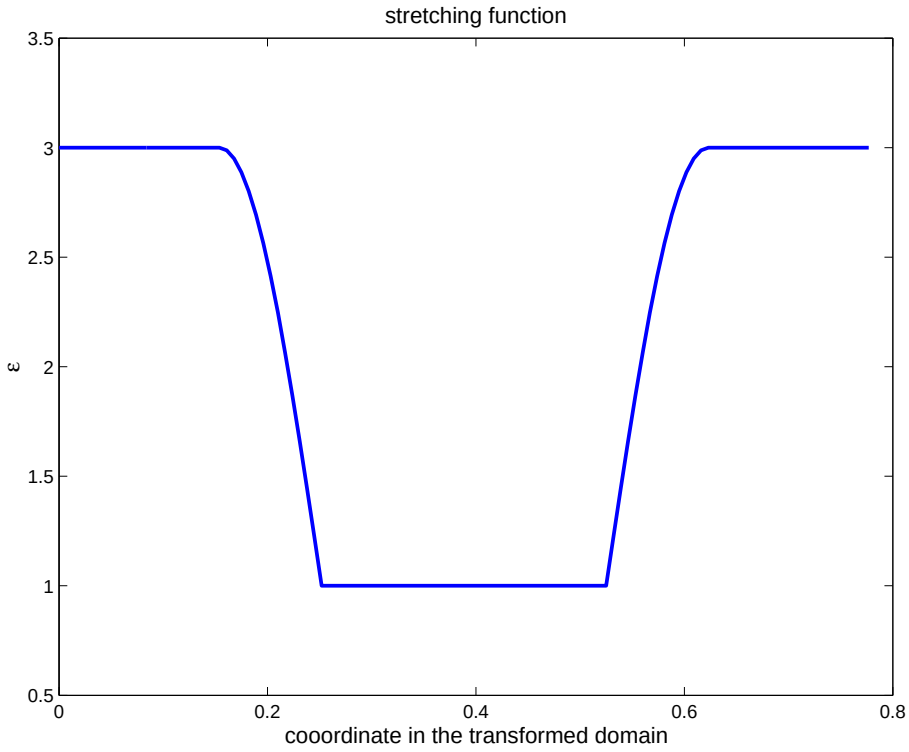


Figure 26: The stretching functions $\epsilon^1(\tilde{x}) = \epsilon^2(\tilde{y})$, used in discretizing the borehole model in Figure 24.

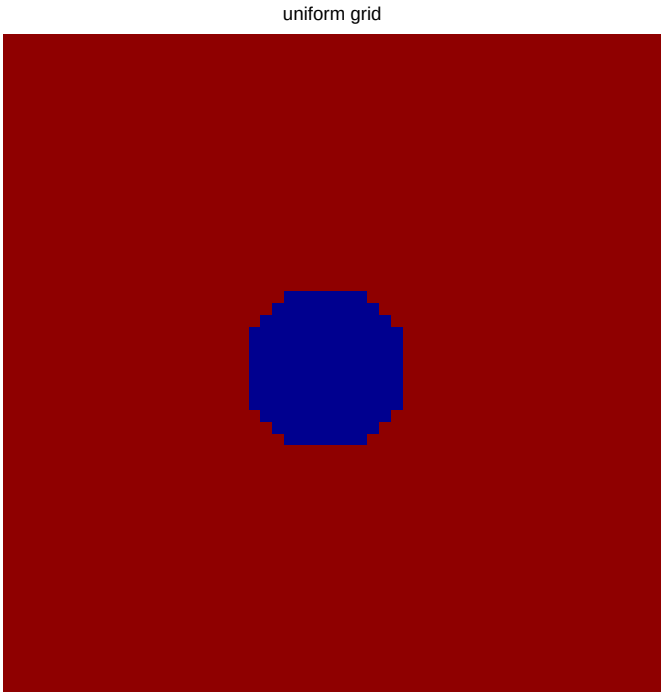


Figure 27: The top view of the discretized borehole using uniform grids with the same grid points used in the stretching grid case (Figure 24). The borehole discretized using the uniform grid mesh is much less smooth and circular than it is in the stretching grid mesh case.

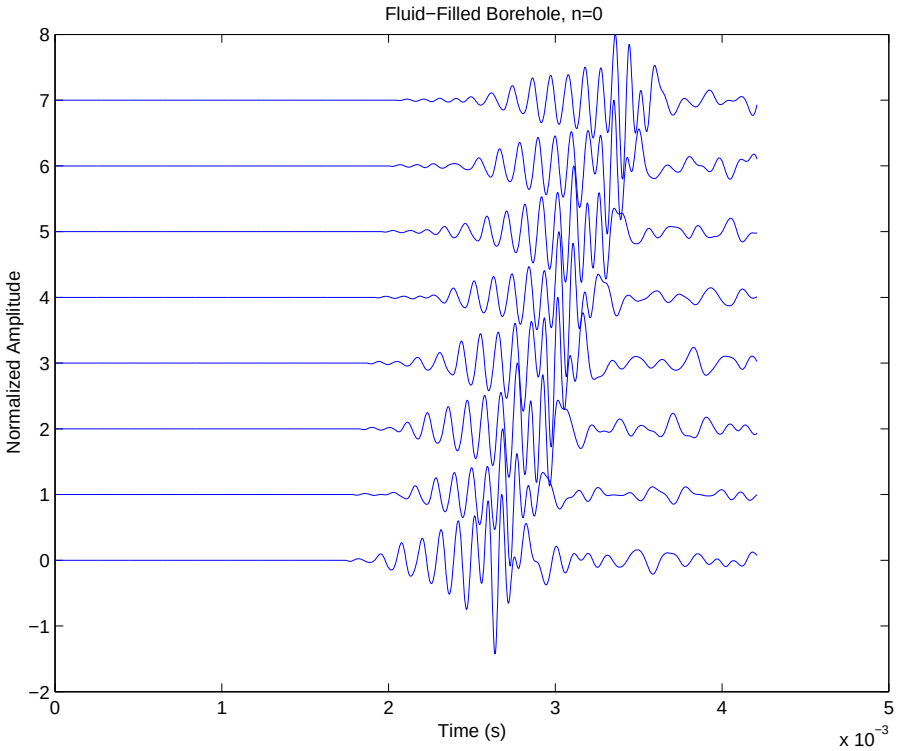


Figure 28: Waveforms from FDTD simulation for the fluid-filled borehole using stretching grids. The spatial differencing scheme is 8th. The source and receivers are at the z axis.

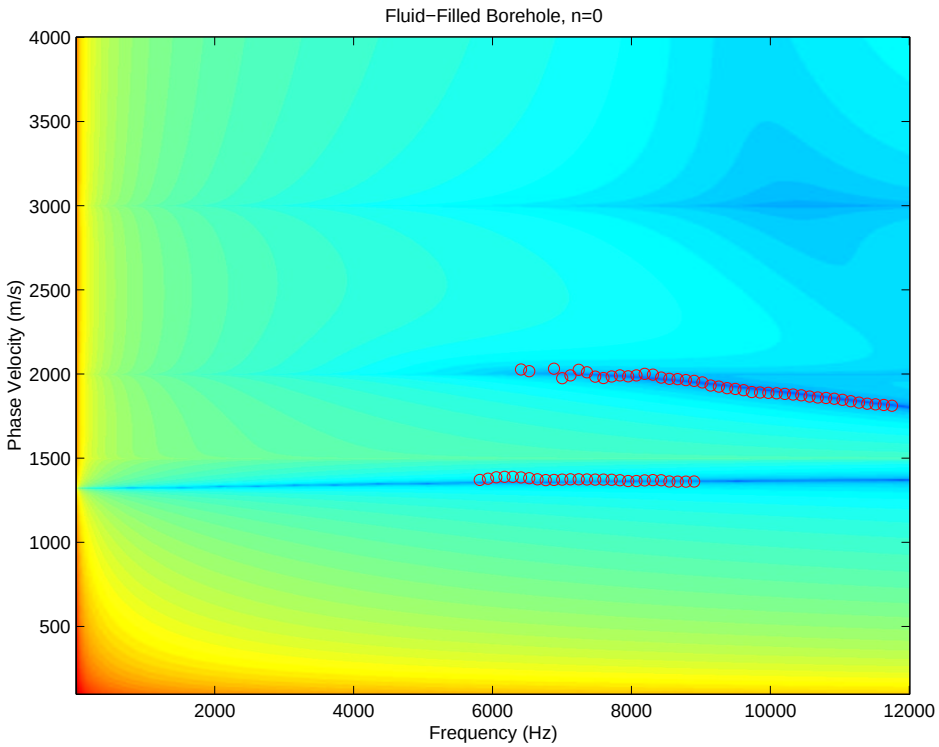


Figure 29: Dispersion curves from analytical solution. The circle lines are from the dispersion analysis of the FDTD results. Two results agree with each other.

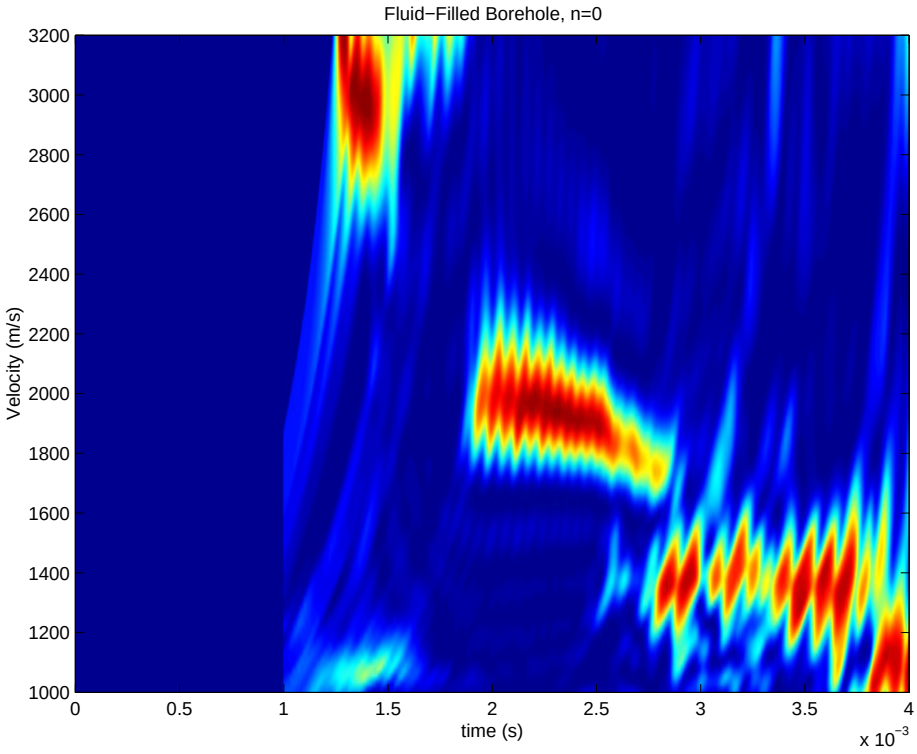


Figure 30: Semblance results of the waveforms obtained from FDTD 28.